Atmospheric
Measurement
Techniques
Open Access
Discussions

OMI tropospheric NO$_2$ air mass factors over South America: effects of biomass burning aerosols

P. Castellanos[1], K. F. Boersma[2,3], O. Torres[4], and J. F. de Haan[2]

[1]Faculty of Earth and Life Sciences, VU University Amsterdam, Amsterdam, the Netherlands
[2]Royal Netherlands Meteorological Institute (KNMI), De Bilt, the Netherlands
[3]Meteorology and Air Quality Group, Wageningen University, Wageningen, the Netherlands
[4]NASA Goddard Space Flight Center, Greenbelt, MD 20771, USA

Correspondence to: P. Castellanos (p.castellanos@vu.nl)

AMTD

8, 2683–2733, 2015

OMI tropospheric NO$_2$ air mass factors over South America

P. Castellanos et al.

Title Page

Abstract	Introduction
Conclusions	References
Tables	Figures

|◄ | ►|

◄ | ►

Back | Close

Full Screen / Esc

Printer-friendly Version

Interactive Discussion

Full Screen / Esc

Printer-friendly Version

Interactive Discussion

Abstract

Biomass burning is an important and uncertain source of aerosols and NO$_x$ (NO + NO$_2$) to the atmosphere. OMI observations of tropospheric NO$_2$ are essential for characterizing this emissions source, but inaccuracies in the retrieval of NO$_2$ tropospheric
5 columns due to the radiative effects of aerosols, especially light-absorbing carbonaceous aerosols, are not well understood. It has been shown that the O$_2$–O$_2$ effective cloud fraction and pressure retrieval is sensitive to aerosol optical and physical properties, including aerosol optical depth (AOD). Aerosols implicitly influence the tropospheric air mass factor (AMF) calculations used in the NO$_2$ retrieval through the
10 effective cloud parameters used in the independent pixel approximation. In this work, we explicitly account for the effects of biomass burning aerosols in the tropospheric NO$_2$ AMF calculation by including collocated aerosol extinction vertical profile observations from the CALIOP instrument, and aerosol optical depth (AOD) and single scattering albedo (SSA) retrieved by the OMI near-UV aerosol algorithm (OMAERUV) in
15 the DISAMAR radiative transfer model for cloud-free scenes. Tropospheric AMFs calculated with DISAMAR were benchmarked against AMFs reported in the Dutch OMI NO$_2$ (DOMINO) retrieval; the mean and standard deviation (SD) of the difference was 0.6 ± 8 %. Averaged over three successive South American biomass burning seasons (2006–2008), the spatial correlation in the 500 nm AOD retrieved by OMI and the
20 532 nm AOD retrieved by CALIOP was 0.6, and 72 % of the daily OMAERUV AOD observations were within 0.3 of the CALIOP observations. Overall, tropospheric AMFs calculated with observed aerosol parameters were on average 10 % higher than AMFs calculated with effective cloud parameters. For effective cloud radiance fractions less than 30 %, or effective cloud pressures greater than 800 hPa, the difference between
25 tropospheric AMFs based on implicit and explicit aerosol parameters is on average 6 and 3 %, respectively, which was the case for the majority of the pixels considered in our study. Pixels with effective cloud radiance fraction greater than 30 % or effective cloud pressure less than 800 hPa corresponded with stronger shielding in the implicit aerosol

correction approach because the assumption of a opaque effective cloud underestimates the altitude resolved AMF; tropospheric AMFs were on average 30–50 % larger when aerosol parameters were included, and for individual pixels tropospheric AMFs can differ by more than a factor of two. The observation-based approach to correcting tropospheric AMF calculations for aerosol effects presented in this paper depicts a promising strategy for a globally consistent aerosol correction scheme for clear sky pixels.

1 Introduction

Satellite observations of backscattered radiation have been vital in measuring and monitoring global scale air pollution, consisting of a mixture of aerosols and reactive gases that are either directly emitted or formed through various chemical and physical processes. These global datasets of atmospheric composition contain important information on the chemistry of the atmosphere (e.g. Stavrakou et al., 2013), trends in air quality (e.g. Castellanos and Boersma, 2012), as well as emissions from fossil fuel burning (e.g. Jaeglé et al., 2005), biogenic hydrocarbon sources (e.g. Marais et al., 2012), lightning (e.g. Bucsela et al., 2010), and biomass burning (e.g. Castellanos et al., 2014). However, the retrieval of tropospheric column amounts of trace gases from satellite observations is complicated and remains a challenge.

In the retrieval of NO_2 tropospheric columns, air mass factors (AMF) are used to derive vertical columns from slant columns that have been calculated from a DOAS (Differential Optical Absorption Spectroscopy) fit to measured radiances or reflectances. The tropospheric AMF is calculated with a radiative transfer model and accounts for the difference in the sun-to-satellite photon path within the troposphere (the slant column) vs. the vertical path from a ground pixel to the top of the troposphere. The AMF is the dominant source of error in retrieving NO_2 tropospheric columns for polluted scenes (Martin, 2002; Boersma et al., 2004), and depends strongly on observable parameters such as the surface albedo, satellite viewing geometry, terrain height, and the pres-

P. Castellanos et al.

Title Page

Abstract	Introduction
Conclusions	References
Tables	Figures

|◄ | ►|
◄ | ►

Back | Close

Full Screen / Esc

Printer-friendly Version

Interactive Discussion

ence of clouds and aerosols, as well as assumed parameters such as the NO_2 profile shape. All of these aspects can give rise to large errors in the AMF calculation and the retrieved NO_2 tropospheric column for individual measurements. In this paper, we will focus on how aerosols, specifically emitted by biomass burning, affect tropospheric AMFs.

In the Dutch OMI NO_2 (DOMINO) retrieval (Boersma et al., 2011), the independent pixel approximation is used to account for the presence of clouds. Thus, the AMF is taken to be a linear combination of a clear-sky AMF and a cloudy AMF.

$$M = wM_{cl} + (1 - w)M_{cr} \tag{1}$$

$$w = \frac{f_{eff}I_{cl}}{f_{eff}I_{cl} + (1 - f_{eff})I_{cr}} \tag{2}$$

In Eq. (1), M is the tropospheric AMF, M_{cl} and M_{cr} are the cloudy and clear-sky AMFs, respectively, and w is the radiance-weighted cloud fraction (Eq. 2) (a function of the effective cloud fraction, f_{eff}; I_{cl} and I_{cr} are the fit window averaged radiances for 100 % cloudy and clear scenes, respectively) (Boersma et al., 2004).

The DOMINO retrieval does not directly take into account the effect of aerosols on the AMF, but instead uses an implicit correction by assuming that the cloud parameters retrieved by the OMI (Ozone Monitoring Instrument) cloud algorithm (OMCLDO2) (Acarreta et al., 2004; Stammes et al., 2008) account for the effect of the aerosols on the light path. The DOMINO retrieval takes the approximation that the effects of aerosols on the tropospheric AMF can be represented as the fractional coverage of a Lambertian reflector that yields a TOA reflectance that best agrees with the observed reflectance, i.e. a radiometrically equivalent, or effective, cloud fraction. Previous work has shown that for OMI the effective cloud fractions retrieved in the O_2–O_2 band are indeed sensitive to aerosols; retrieved cloud fractions were higher and cloud pressures were lower in the presence of aerosols compared to a pure molecular scattering atmosphere, and aerosol optical depth (AOD) was strongly correlated with effective cloud fraction, especially for strongly scattering aerosols (Boersma et al., 2004, 2011). For

a few synthetic cases of assumed aerosol type and optical depth, Boersma et al. (2004) showed that the tropospheric AMF could increase by as much as 40 % when aerosol radiative effects are directly accounted for. This raises the following question: to what extent can the implicit correction via the retrieved cloud parameters mimic the effects

5 of different observed aerosol concentrations, vertical aerosol distributions, and physical aerosol properties?

Compared to a pure molecular scattering atmosphere, the presence of a scattering component, whether aerosol or cloud, can change light paths as well as their contributions to the top of the atmosphere (TOA) reflectance. In some aspects, the radiative

10 effects of scattering aerosols and clouds are comparable. Both aerosols and clouds decrease the sensitivity to an absorber at lower altitudes, as more photons will be scattered back to the satellite before reaching the surface, a shielding effect. Moreover, clouds and aerosols also increase the sensitivity to an absorber above the scattering layer, by increasing the contribution of these light paths to the TOA reflectance, i.e. an

15 albedo effect. While these effects can be approximated by the effective cloud model, an opaque Lambertian surface with high albedo (Koelemeijer and Stammes, 1999) (i.e. the altitude dependent AMFs (Eskes and Boersma, 2003) or scattering weights (Palmer et al., 2001) below a cloud are zero), aerosols can modify the radiative transfer in ways that may not be adequately covered by this model.

20 Because aerosols and trace gases are often well mixed near the surface, aerosols can increase the sensitivity to an absorber as a result of multiple scattering, which increases the light path and thus trace gas absorption in the pollution layer compared to a Rayleigh atmosphere. The effect of aerosols and clouds will also differ in the case of absorbing aerosols, which will decrease the sensitivity to an absorber by decreasing

25 the number of photons that return to the satellite from within and below the aerosol layer. Finally, due to their different characteristic sizes (cloud particles being larger), aerosol and cloud particles have different phase functions. Thus, an accurate estimate of the height and physical properties of an aerosol layer with respect to the vertical

OMI tropospheric NO₂ air mass factors over South America

P. Castellanos et al.

Full Screen / Esc

Printer-friendly Version

Interactive Discussion

distribution of the absorber is essential for accurate air mass factor calculations for trace gas retrievals (Leitão et al., 2010).

Lin et al. (2014) studied the effect of aerosols on OMI NO_2 tropospheric column retrievals at three urban/suburban MAX-DOAS measurement sites in East China by implementing aerosol optical depth (AOD) from AERONET or MAX-DOAS observations, and aerosol physical properties (single scattering albedo (SSA) and phase function) and vertical profiles from the GEOS-Chem chemical transport model in the AMF calculation, and explicitly corrected the O_2–O_2 cloud retrieval for the presence of aerosols. With their aerosol-corrected O_2–O_2 cloud parameters, and in situations with the AOD exceeding 0.8, their tropospheric AMF was significantly higher than the DOMINO v2 retrieval, and the NO_2 tropospheric column was 70–90 % lower when aerosol effects are included. However, when averaged over thirty days, the explicit correction for aerosols resulted in NO_2 tropospheric columns that were only 14 % lower than the original DOMINO v2 retrieval.

In this work, we investigated the properties of the implicit aerosol correction for tropospheric NO_2 retrievals from OMI in the case of active biomass burning in South America, which generates elevated concentrations of reactive gases and aerosols. South America contributes on average approximately 5 % of total global annual burned area, but 15 % of total global annual biomass burning carbon emissions (Giglio et al., 2010; van der Werf et al., 2010) due to the high fuel loading and combustion completeness of deforestation burning along the borders of the Amazon. Bottom-up estimates of biomass burning NO_x emissions are largely uncertain due to uncertainties in the static emission factors used to convert biomass consumed into NO_x emitted. New parameterizations based on top-down estimates of NO_x emissions from OMI NO_2 observations have been proposed as a way to better characterize the variability in biomass burning NO_x emission factors (Mebust et al., 2011; Schreier et al., 2014). In this paper, we focus on areas of active burning to analyze whether the effects of aerosols on NO_2 tropospheric AMFs could influence these top-down estimates.

In our analysis we compared NO_2 tropospheric AMFs from the DOMINO v2 algorithm to AMFs calculated with explicit aerosol scattering and absorption in the radiative transfer calculations. To describe the aerosol optical properties in the AMF calculations, we utilized measurements of AOD and SSA retrieved from simultaneous OMI measurements in the UV (OMAERUV algorithm, Torres et al., 2013), as well as collocated aerosol extinction vertical profile measurements from the Cloud-Aerosol Lidar with Orthogonal Polarization (CALIOP) instrument (Winker et al., 2010). While previous studies have relied on models or ancillary point measurements, such as MAX-DOAS or AERONET, to analyze the effects of aerosols on tropospheric NO_2 retrievals, our approach is novel in that it exploits globally available satellite measurements. This allows for the analysis of the OMI data record over large spatial and temporal scales, and potentially for a globally consistent observation-based explicit aerosol correction.

2 Satellite observations and radiative transfer modeling

2.1 The Ozone Monitoring Instrument (OMI)

OMI is a nadir viewing imaging spectrometer aboard the EOS Aura satellite that measures backscattered radiation in the UV-Vis from 270 to 500 nm (Levelt et al., 2006). During the first three years of operation starting in 2004, OMI provided daily global coverage at a nominal resolution of 13 km × 24 km for nadir pixels. In mid-2007, what is probably an external obstruction began affecting the quality of the radiance observations of all wavelengths at specific viewing angles. Each viewing angle corresponds to a row on the OMI 2-D CCD detector. Hence, the degradation of the OMI data quality for some viewing angles is referred to as the row-anomaly. Currently, approximately half of the sensor's viewing angles are affected by the row-anomaly (Braak, 2010).

Full Screen / Esc

Printer-friendly Version

Interactive Discussion

2.2 OMI effective cloud fraction and cloud pressure retrieval (OMCLDO2)

The O$_2$–O$_2$ effective cloud fraction formulation assumes the observed TOA reflectance between 460 and 490 nm can be represented by a linear combination of the cloudy and clear sky fractions of the pixel (Eq. 3), where the cloud is modeled as an opaque Lambertian reflector with albedo equal to 0.8 (Acarreta et al., 2004; Stammes et al., 2008).

$$R = f_{eff}R_{albedo=0.8} + \left(1 - f_{eff}\right)R_{cr} \qquad (3)$$

In Eq. (3), R is the simulated reflectance best matching the observed reflectance, f_{eff} is the effective cloud fraction, $R_{albedo=0.8}$ is the simulated reflectance for a Lambertian cloud with albedo equal to 0.8, and R_{cr} is the clear-sky reflectance. A cloud albedo of 0.8 was chosen to compensate for the missing transmission of the opaque Lambertian cloud model (Stammes et al., 2008).

The retrieval spectral window includes the collision induced absorption feature of oxygen (O$_2$–O$_2$) at 477 nm. In the presence of clouds, O$_2$–O$_2$ complexes below the cloud are shielded, and because oxygen is well mixed, the observed O$_2$–O$_2$ slant column is a measure of the height of the cloud.

A DOAS fit of the OMI reflectance spectrum is used to derive the continuum reflectance at the reference wavelength of 475 nm and the O$_2$–O$_2$ slant column. Combined with the viewing geometry, solar geometry, and surface properties, these values are converted to an effective cloud fraction and pressure with the aid of a look-up table (LUT) produced with the doubling-adding KNMI (DAK) v3.0 radiative transfer model. In the retrieval, the surface albedo for the simulation of the clear-sky reflectance is taken from the Kleipool et al. (2008) climatology.

O$_2$–O$_2$ absorption is a function of the square of the O$_2$ number density. As a consequence, the TOA radiance measured by OMI is a function of the inverse of the temperature vertical profile. Because the LUT was derived using a mid-latitude summer temperature profile in the DAK radiative transfer calculations, there is a systematic error in

the retrieved cloud pressures when the actual temperature profile deviates significantly from the standard mid-latitude summer atmosphere. If the actual temperature is significantly lower than the mid-latitude summer profile, the O$_2$–O$_2$ effective cloud pressure overestimates the true cloud pressure, and vice versa. In Maasakkers (2013), the magnitude of this error was found to be ±0–100 hPa, within the estimated accuracy of the effective cloud pressure retrieval as shown in a comparison to MODIS and CLOUDSAT observations (Sneep et al., 2008).

2.3 Dutch OMI NO$_2$ (DOMINO) retrieval algorithm

In the Dutch OMI NO$_2$ retrieval algorithm, NO$_2$ tropospheric vertical column densities are derived in three steps. First, a DOAS fit is used to obtain NO$_2$ slant columns from OMI reflectance measurements in the 405–465 nm range assuming a fixed temperature of 221 K for the absorption cross section of NO$_2$ (Vandaele et al., 1998). For a discussion of the fitting method, and improvements therein, we refer to van Geffen et al. (2014). Next, the stratospheric contribution to the slant column is estimated by assimilating measured NO$_2$ slant columns in the TM4 global chemistry and transport model (Dirksen et al., 2011). After subtracting the stratospheric slant column from the total slant column, the remaining tropospheric slant column is converted to a vertical column by dividing by the tropospheric AMF.

In DOMINO v2 (Boersma et al., 2011), the cloudy (M_{cl}) and clear-sky (M_{cr}) tropospheric AMFs are derived by first interpolating a LUT of altitude-resolved AMFs (m_l) that were pre-calculated with the DAK radiative transfer model. The altitude-resolved AMFs represent the ratio of the partial slant column density to the partial vertical column density for an atmospheric layer. The altitude-resolved cloudy and clear-sky AMFs are weighted by a corresponding TM4 vertical profile of tropospheric NO$_2$-subcolumns ($x_{a, l}$) (Eqs. 4 and 5) to derive the cloudy and clear-sky tropospheric AMFs.

The altitude-resolved AMFs in the LUT are represented as a function of six forward model parameters (b): (1) solar zenith angle, (2) viewing zenith angle, (3) relative azimuth angle, (4) surface albedo, (5) terrain height, and (6) layer pressure. The clear-

sky altitude-resolved AMFs are derived by interpolating the LUT to a terrain height and surface albedo taken from a Global 3 km Digital Elevation Model and the Kleipool et al. (2008) surface albedo climatology, respectively. Together with the satellite viewing geometry and TM4 pressure levels, this corresponds to the forward model parameters b_{cr}. For the cloudy-sky altitude-resolved AMFs, the "terrain height" is approximated by the retrieved O_2–O_2 effective cloud top pressure, and the "surface albedo" for that terrain is equal to 0.8 (b_{cl}) (Stammes et al., 2008).

$$M_{cl} = \frac{\sum_l m_l(b_{cl}) x_{a,l} c_l}{\sum_l x_{a,l}} \qquad (4)$$

$$M_{cr} = \frac{\sum_l m_l(b_{cr}) x_{a,l} c_l}{\sum_l x_{a,l}} \qquad (5)$$

$$c_l = \frac{221 - 11.4}{T_l - 11.4} \qquad (6)$$

In Eqs. (4–6), c_l is an a posteriori correction factor to account for the temperature difference between the effective temperature in the TM4 NO_2-subcolumn (T_l) and 221 K, which was assumed for the NO_2 cross section during the DOAS slant column fitting. T_l is based on ECMWF meteorological data fields that are used to drive the TM4 simulations of the vertical NO_2 profile. Together with the radiance-weighted effective cloud fraction, M_{cl} and M_{cr} are used in the independent pixel approximation (Eq. 1) to calculate the overall tropospheric AMF.

In deriving the altitude-resolved AMF LUT with DAK, surface reflectivity was assumed to be Lambertian, and the atmosphere plane-parallel, but polarization was accounted for. The temperature and pressure vertical profiles corresponded to the AFGL mid-latitude summer profile.

Comparisons to MAX-DOAS observations (Irie et al., 2012; Ma et al., 2013) have shown that DOMINO v2 NO_2 tropospheric columns are highly correlated with the surface observations ($R = 0.91$–0.93), but are biased low by approximately 10–15 %. OMI

NO$_2$ tropospheric column observations have been used extensively to study surface NO$_x$ emissions (e.g. Vinken et al., 2014), NO$_x$ atmospheric lifetimes (e.g. Beirle et al., 2011), and air quality trends (e.g. de Ruyter de Wildt et al., 2012).

2.4 OMI AOD and SSA retrieval (OMAERUV)

The OMAERUV algorithm retrieves aerosol extinction optical depth (AOD) and single scattering albedo (SSA) at 388 nm, for cloud-free scenes (Torres et al., 2013, 2007). Converted values at 354 and 500 nm are also reported. Clear sky conditions are required to reliably retrieve AOD and SSA, because reflectance from clouds causes errors in the retrieved aerosol parameters. Thus, strict cloud filtering is implemented in the algorithm (see Appendix A for details regarding the cloud filtering criteria).

The retrieval algorithm makes use of the relationship between the 354-to-388 nm spectral contrast and the 388 nm reflectance to derive the AOD and SSA at 388 nm, while the 354 and 500 nm products are obtained by converting the 388 nm product using the spectral dependence of the prescribed aerosol type and particle size distribution. The OMAERUV algorithm assumes that the column aerosol can be represented by one of three main aerosol types: dust, carbonaceous aerosol associated with biomass burning, or weakly absorbing sulfate based aerosol. The particle size distributions of the three types are based on long-term statistics from AERONET (Aerosol Robotics Network, Holben et al., 1998). The algorithm uses a LUT of reflectances at 354 and 388 nm that were calculated for each aerosol model using a radiative transfer model. The LUT has nodal points in AOD, SSA, aerosol layer height (ALH), surface pressure, and viewing geometry.

In a recent improvement to the OMAERUV algorithm, a new scheme was implemented to prescribe the aerosol type based on collocated AIRS CO observations, UVAI, and geographical location. Depending on the aerosol type, a best guess ALH is also prescribed. For the case of carbonaceous aerosols with aerosol index greater than 0.5, the ALH is inferred from a multiyear climatology of ALH that was developed from CALIOP backscatter vertical profile measurements (Torres et al., 2013), otherwise

the ALH is assumed to be 1.5 km. The vertical profile of aerosol extinction is modeled as a Gaussian distribution that peaks at the ALH and has a 1 km half-width. For sulfate-based aerosols, the algorithm assumes that the aerosol concentration decreases from the surface in an exponential decay with 2 km scale height.

The OMAERUV standard level 2 data product consists of a final estimate for AOD and SSA consistent with the prescribed best guess ALH described above. The level 2 data product also provides the AOD and SSA that would have been retrieved at the five ALH nodal points (0, 1.5, 3.0, 6.0, and 10 km) of the LUT. Thus, one can interpolate the AOD and SSA to an ALH other than the best guess ALH if better information on the ALH is available, such as (instead of the climatology) simultaneous observations from CALIOP.

In a comparison to AOD observations at 44 AERONET sites around the world, Ahn et al. (2014) found that for 65 % of the observations, the difference between AERONET and OMAERUV AOD was less than 30 %, the expected uncertainty of the retrieval. Overall, for carbonaceous aerosols, the slope and y-intercept of the regression between OMAERUV and AERONET AOD were 0.74 and 0.15, respectively, with a correlation coefficient of 0.81. OMAERUV SSA has also been compared to AERONET retrievals (Jethva et al., 2014). The OMI SSA product agrees with AERONET to within 0.03 in 50 % of the matched pairs, and to within 0.05 in 75 % of the cases.

2.5 CALIOP aerosol extinction vertical profiles

CALIOP is a dual wavelength polarization lidar on board the CALIPSO satellite that measures attenuated backscatter at 532 and 1064 nm at a vertical resolution of 30 m below 8.2 km, and 60 m up to 20.2 km (Winker et al., 2013). Along the orbital track, CALIOP has a horizontal resolution of 335 m. Observations are available from mid June 2006. The CALIOP level 2 products include a vertical feature mask that characterizes atmospheric layers as containing cloud, aerosol, or clean air. Cloud and aerosol are detected with a threshold technique (Vaughan et al., 2009), and a discrimination algorithm (Liu et al., 2009) assigns a cloud-aerosol discrimination (CAD) score to each

layer. The CAD score is a percentile between −100 and 100 representing the probability that a layer contains cloud (positive CAD score) or aerosol (negative CAD score). Thus a CAD score of −100 means that the layer is certain to contain aerosol. For aerosol layers, the retrieval algorithm selects an aerosol type (Omar et al., 2009). The backscatter ratio for that type (the ratio of aerosol 180-backscatter to extinction) is used to retrieve aerosol extinction (Young and Vaughan, 2009).

For this work, we used daytime CALIOP level 2 532 nm aerosol extinction vertical profiles that were collocated with DOMINO and OMAERUV retrievals. Although the algorithm accounts for signal attenuation above a layer, strong absorption by black carbon at 532 nm can diminish the sensitivity to aerosols near the surface (Torres et al., 2013) adding uncertainty to the retrieved aerosol extinction in these layers. However, in our analysis of NO₂ tropospheric AMFs, the choice of aerosol extinction at 532 nm over 1064 nm (where absorption is weaker) did not significantly affect the results ($< 5\%$ difference, unbiased). We compared the 532 nm and 1064 aerosol extinction vertical profiles by calculating an aerosol extinction weighted average altitude, i.e. an effective ALH, for each retrieval (Eq. 7). In Eq. (7), $h(l)$ and $\sigma(l)$ are the CALIOP altitude and aerosol extinction of layer l, respectively. The ALH derived at the two wavelengths was within 150, 500 m, and 1 km for 47, 90, and 99 % of the pixels considered, respectively (Fig. S1 in the Supplement).

$$\text{ALH} = \frac{\sum h(l)\sigma(l)}{\sum \sigma(l)} \tag{7}$$

When CALIPSO was launched, the time difference between OMI and CALIOP overpass was 13 min, but is currently approximately 8 min. Unfortunately, due to the progression of the OMI row anomaly, useful collocated OMI-CALIOP data are scant beyond December 2008.

A comparison of CALIOP observations to ground-based LIDAR showed that the top and base height of aerosol and cloud layers of the two measurements generally agreed to within 0.1 km, indicating that the CALIOP cloud-aerosol discrimination algorithm can

provide reliable information on the vertical profile of aerosols (Kim et al., 2008). In general, analysis of co-located MODIS and CALIOP AOD retrievals indicate that CALIOP AOD is higher than MODIS, but the two observations are roughly within the combined expected uncertainty (Winker et al., 2013).

2.6 Satellite data selection and OMI-CALIOP colocation

As we are interested in retrievals affected by biomass burning emissions, we filtered the OMI observations within our South American domain (36° S to 14° N and 84° W to 30° W) for pixels where MODIS-Aqua reported an active fire between July and November (the South American burning season) in 2006–2008 (Fig. 1). DOMINO pixels were selected if the "tropospheric column flag" was equal to zero (indicating a reliable retrieval). OMAERUV pixels were selected if the "algorithm quality flag" was equal to zero, indicating cloud screened ("most reliable") retrievals.

We created a dataset of OMI-CALIOP collocated pixels by averaging together all daytime CALIOP extinction vertical profiles within 0.5° of the OMI pixel center. We selected aerosol layers where the CAD score was less than –20, QC-flag equal to 0 or 1, and the extinction uncertainty was less than 99.9 (this value indicates a failed retrieval).

In Fig. 1 we show DOMINO v2.0 NO_2 tropospheric columns, MODIS-Aqua active fires, OMAERUV AOD, and CALIOP AOD averaged over 2006–2008. Over the three fire seasons, there were in total 13 356 OMI-CALIOP collocated pixels. In general, the highest observed tropospheric NO_2 and AOD occur in central and western Brazil, eastern Bolivia, and Paraguay, locations with the most active fires. The three-year average AOD measured by CALIOP at 532 nm and OMAERUV at 500 nm generally follow the same spatial patterns. The spatial correlation coefficient between the two 3 year averages is 0.61 ($N = 5803$). The OMAERUV AOD at 500 nm is on average 30 % lower than the CALIOP AOD at 532 nm, reflecting the sub-pixel sampling of CALIOP, the spectral dependence of the AOD, and differences in vertical sensitivity and the aerosol models used in the two retrievals.

Because OMAERUV retrieved AOD and SSA is sensitive to the prescribed ALH, we derived new estimates of AOD and SSA that reflect the CALIOP observed vertical distribution of aerosols. Figure 2 shows the probability distributions of the OMAERUV prescribed ALH and the CALIOP effective ALH over South America for biomass burning aerosols. For pixels where OMAERUV assigns an ALH equal to zero, this corresponds to an aerosol vertical profile with a maximum at the surface that decays exponentially with a 2 km scale height. In Fig. 2 this is depicted as an ALH equal to 1.88, which is the effective ALH for such a profile. The mean CALIOP effective ALH is 1.5 km, the same default value that is utilized for carbonaceous aerosols in the OMAERUV retrieval. However, there is substantial variability in the daily observations, which show that 50 % of the observations have an ALH less than 1.5 km.

Figure 3 shows the average shape of the observed CALIOP aerosol extinction vertical profile and the collocated simulated TM4 NO_2 profile for three ranges of CALIOP effective ALH: less than 1 km, 1–2 km, and greater than 2 km. This plot was made by scaling all extinction vertical profiles to an AOD of 0.5 and tropospheric NO_2 profiles to a vertical column equal to 1 before averaging by layer. In general, the bulk of the NO_2 is concentrated between the surface and roughly 2 km or 800 hPa, which is expected because we have selected pixels that contain active fires (i.e. a nearby surface source). When the effective ALH is less than 1 km, the aerosol and NO_2 tend to follow the same profile shape and are well mixed together. Both profiles peak at the surface, indicating a common nearby surface source. When the effective ALH is 1–2 km, aerosols are well mixed from the surface to 2 km, while the NO_2 continues to peak at the surface. This may be a result of the shorter lifetime of NO_2, underestimated buoyant plume rise in the model, or both. Figure 3 also shows that an effective ALH greater than 2 km corresponds to less aerosol extinction near the surface and an elevated extinction peak at 2–3.5 km, indicative of regional transport. The NO_2 concentration in the model profile is somewhat enhanced above 2 km as well (compared to the other two NO_2 profiles), but the peak in NO_2 concentration remains at the surface, a consequence of the shorter lifetime of NO_2.

OMI tropospheric NO$_2$ air mass factors over South America

P. Castellanos et al.

Title Page

Abstract | Introduction

Conclusions | References

Tables | Figures

|◄ | ►|

◄ | ►

Back | Close

Full Screen / Esc

Printer-friendly Version

Interactive Discussion

P. Castellanos et al.

We replaced the OMAERUV prescribed climatological ALH with observed CALIOP effective ALHs to obtain an estimate of the SSA and AOD that better reflects the daily variability of the aerosol vertical profile. We interpolated the OMAERUV AOD and SSA given on the 5 altitude nodal points to the CALIOP ALH (Fig. 4). On average, the AOD interpolated to the effective ALH was 7 % higher than the AOD derived from the OMAERUV prescribed ALH. There was on average no change in the SSA. Small increases in AOD are expected because although the OMAERUV assumed aerosol layer heights are generally consistent with the CALIOP observations, CALIOP observations indicate that more profiles have enhanced aerosol extinction closer to the surface (Fig. 2).

When collocated daily measurements are compared, the slope between CALIOP 532 nm AOD and OMAERUV 500 nm AOD is 0.65 and the correlation coefficient is 0.57. Figure 5 shows daily OMAERUV AOD measurements after adjusting for the CALIOP ALH. The slope increases to 0.70, comparable to the slope from the OMAERUV-AERONET evaluation discussed in Sect. 2.3, but there is no change in the correlation coefficient. For both choices of ALH, 72 % of the OMAERUV AOD observations were within 0.3 of the CALIOP observations.

Because the CALIOP footprint samples only a fraction of the OMI pixel, we can expect scatter in the comparison of the OMAERUV and CALIOP AOD, and that the AOD derived from CALIOP will likely not be as representative of the AOD for the DOMINO viewing scene as the OMAERUV AOD. The OMAERUV observations also provide the spectral information needed to calculate the AOD at the DOMINO reference wavelength. For these reasons, we scaled the CALIOP aerosol extinction vertical profiles to the OMAERUV AOD in our analysis. Thus, in our analysis CALIOP observations provide the aerosol vertical profile shape, but the AOD and SSA are based on OMI observations.

2.7 Calculation of altitude resolved air mass factors

Altitude resolved AMFs were computed with the DISAMAR (Determining Instrument Specifications and Analyzing Methods for Atmospheric Retrieval) radiative transfer model (de Haan, 2011). DISAMAR was designed to simulate retrievals of properties of atmospheric trace gases, aerosols, clouds, and the ground surface for passive remote sensing observations. Similar to the DAK radiative transfer model used to derive the DOMINO LUT, DISAMAR computes the reflectance and transmittance in the atmosphere using the polarized doubling-adding method (de Haan et al., 1987). This method calculates the internal radiation field in the atmosphere for an arbitrary number of layers, in which Rayleigh scattering, gas absorption, and aerosol and cloud scattering and absorption can occur. A key difference between DAK and DISAMAR is that DISAMAR utilizes a separate altitude grid for the radiative transfer calculations that is independent of the grid used for specifying the atmospheric properties. This is important for simulating strong vertical gradients in the radiation field, e.g. near the top of clouds.

In Fig. 6, we show the comparison of NO_2 tropospheric AMFs from DOMINO v2.0 (based on the DAK-derived LUT) and DISAMAR for all retrievals with active fires in our South America domain ($N = 71\,618$). Identical to the DAK calculations for the DOMINO retrieval, in DISAMAR the altitude resolved AMF was calculated at 439 nm and the surface reflectance was taken to be Lambertian and the atmosphere plane-parallel. However, in our analysis instead of interpolating the AMF from a LUT with fixed reference points for viewing geometry, albedo, and surface pressure for each OMI pixel we simulated the radiative transfer online using the exact values of surface albedo, effective cloud fraction and pressure, viewing geometry, and temperature, pressure, and NO_2 profiles from the DOMINO product.

The differences between the DOMINO and DISAMAR tropospheric AMFs in Fig. 6 represent the errors that arise from interpolating the LUT in the DOMINO retrieval, and numerical differences that arise from higher resolution vertical layering in the DISAMAR

radiative transfer calculations. On average, tropospheric AMFs calculated in DOMINO v2.0 using the LUT approach are nearly equivalent to on-line radiative transfer modeling with DISAMAR, as the differences in tropospheric AMF derived from the two methods are on average -0.005 (-0.6%); tropospheric AMFs vary from ~ 0.5 to ~ 2.5. However, for individual measurements the errors are larger as the SD of the differences is 0.086 (8 %), putting an upper bound on this error of approximately 20 %. Henceforth, we will refer to the DISAMAR retrieval implementing the DOMINO configuration as DISAMAR-standard.

In order to model aerosol absorption and scattering effects explicitly, we took SSA and AOD from OMAERUV retrievals, and aerosol extinction vertical profiles from co-located CALIOP observations. In the retrievals with explicit aerosol effects, for each pixel we used the DOMINO viewing geometry, surface albedo, and temperature, pressure, and NO_2 vertical profiles, but excluded the DOMINO cloud parameters, because we assume each OMAERUV scene is cloud free, as we only consider OMAERUV retrievals with algorithm quality flag equal to zero. Although we are only able to analyze ostensibly cloud-free pixels, the strength of this approach is that the AOD, SSA, and NO_2 slant columns and AMFs are derived from identical scenes.

We do not expect residual cloud contamination to significantly affect our results because we limited our analysis to pixels where active fires are detected by MODIS-Aqua, and clear skies facilitate favorable conditions for open burning. An additional check was made by comparing the AOD measured by CALIOP including detected cloud layers (CAD scores < -20 and > 20). The increase in AOD was negligible ($< 0.1\%$). After implementing the active fire filter, effective cloud radiance fractions (that arise due to the effects of aerosols on TOA reflectance in the O_2–O_2 band) do not exceed 50 %, the threshold typically implemented when analyzing NO_2 tropospheric columns.

In DISAMAR, the Ångström exponent calculated from the OMAERUV AOD at 388 and 500 nm gives the spectral dependence of the AOD. Aerosol scattering was modeled by the Henyey–Greenstein phase function with an asymmetry parameter of 0.7, consistent with the biomass burning aerosol models used in the OMAERUV retrieval,

Full Screen / Esc

Printer-friendly Version

Interactive Discussion

as well as long-term statistics from AERONET observations in Brazil (Dubovik et al., 2002). We will refer to these retrievals as DISAMAR-aerosol.

3   Results: OMI NO$_2$ air mass factors with explicit aerosol effects

In Fig. 7 we show the comparison of tropospheric AMFs calculated with the DISAMAR-standard and DISAMAR-aerosol retrievals for all 13 356 OMI-CALIOP collocated pixels over South America. Tropospheric AMFs are on average 11 % higher when OMAERUV and CALIOP aerosol characteristics (instead of effective O$_2$–O$_2$ cloud parameters) are implemented in the retrieval. The asymmetrical probability distribution of the differences in AMF has a peak at 0.04. Approximately 66 % of the pixels differ by less than ±0.2 (18 %), within the 20 % estimated lower limit for the AMF uncertainty for polluted scenes (Boersma et al., 2004). The remaining roughly 34 % of the pixels lie in the positive tail of the probability distribution. In the following, we will analyze the retrieval conditions that generate small and large differences in the tropospheric AMF.

Figure 8 shows typical altitude resolved AMFs, CALIOP aerosol extinction profiles, and simulated TM4 NO$_2$ profiles for two pixels where the difference in tropospheric AMF is less than ±0.2 (i.e. when the implicit aerosol correction generates tropospheric AMFs that agree reasonably well with AMF calculations that include observed aerosol parameters). Figure 9 shows the same data for two pixels where the difference is greater than ±0.2 (i.e. where the implicit aerosol correction fails).

In Fig. 8, the difference in the tropospheric AMFs is small because the implicit aerosol correction reasonably approximates the shape of the altitude resolved AMFs calculated with observed aerosol parameters. The difference in the tropospheric AMF is primarily driven by the discontinuity in the altitude resolved AMF introduced by the effective cloud (Eq. 1). The altitude resolved AMF represents the change in the logarithm of the TOA reflectance when a unit amount of NO$_2$ is added to the atmosphere at the altitude considered. Adding NO$_2$ below an opaque cloud will not affect the reflectance. Therefore, the altitude resolved AMF below the cloud is zero. When aerosol effects are

considered explicitly, the reduction in AMF towards the surface occurs more gradually compared to the opaque cloud because generally aerosols are not concentrated in a single optically thick layer and aerosol scattering within the aerosol layer increases sensitivity to NO_2.

Comparing Figs. 8 and 9, the factors that distinguish retrievals with large differences from those with small differences in tropospheric AMFs are lower effective cloud pressure, higher effective cloud fraction, and higher AOD. Also, in pixels where the effective cloud correction fails (Fig. 9), the O_2–O_2 effective cloud pressure is typically above or at the top of the aerosol layer and the effective cloud shields a larger fraction of the atmosphere. Figure 9 also shows that because the AOD and effective cloud fraction are strongly correlated, the higher AOD in the pixels where the effective cloud correction fails results in a larger weighting of the cloudy component of the tropospheric AMF, and a lower altitude resolved AMF within the aerosol layer (Eq. 1).

In Fig. 10, we binned the differences in tropospheric AMF (DISAMAR-aerosol – DISAMAR-standard) for all 13 356 pixels considered according to the difference between the O_2–O_2 effective cloud pressure and the CALIOP effective aerosol layer pressure (ALP), the OMAERUV AOD, the O_2–O_2 effective cloud pressure, and the O_2–O_2 effective cloud radiance fraction. For the majority of the pixels (73 %), the O_2–O_2 effective cloud pressure and the CALIOP effective ALP were within 150 hPa. As the reduction in sensitivity to NO_2 occurs at approximately the same height in the two retrievals, the implicit aerosol correction yields a tropospheric AMF that is on average within 20 % of the AMF calculated with explicit aerosol effects. In general, if the O_2–O_2 effective cloud pressure is greater than 800 hPa (56 % of pixels), the difference in tropospheric AMF is on average less than ∼ 10 % (Fig. 10c) because the CALIOP effective ALP tends to be within 100 hPa (Fig. 11).

Figure 10b and d show that for the approximately 70 % of pixels where the AOD was less than 0.6 and the effective cloud radiance fraction was less than 30 %, the difference in AMF was on average also less than ∼ 10 %. This indicates that for low AOD conditions the majority of the tropospheric AMF is derived from the clear sky fraction

of the pixel and errors in the implicit aerosol correction are minimal. Overall, because the effective cloud correction generally overestimates shielding within the aerosol layer, even for pixels with low AOD, low effective cloud fraction, and an effective cloud pressure close to the CALIOP ALP, the DISAMAR-aerosol AMF tends to be larger, albeit by on average 3–6 %. An overview of the ranges in observable parameters where the implicit aerosol approach yields tropospheric AMFs within 20 % of AMFs based on observed aerosol parameters can be found in Table 1.

The largest mean differences between the DISAMAR-aerosol and DISAMAR-standard retrieval occur for O_2–O_2 effective cloud pressures more than 150 hPa lower than the CALIOP effective ALP (approximately 24 % of the pixels) (Fig. 10a), and for AODs greater than 0.6 (approximately 30 % of the pixels) (Fig. 10b). These situations correspond with significantly stronger screening in the effective cloud approach compared to AMF calculations based on observed aerosol parameters. The DISAMAR-aerosol tropospheric AMF for these low effective cloud pressure pixels is on average 30–50 % higher than the DISAMAR-standard AMF, but can be more than a factor of 2 higher for individual pixels.

Uncertainties in the observed aerosol parameters used in the DISAMAR-aerosol tropospheric AMF calculations can account for only part of the 30–50 % average difference between the DISAMAR-standard and DISAMAR-aerosol calculations for high AODs (> 0.6) (see Appendix B); the upper limit of the combined uncertainties in retrieved aerosol parameters is 25–30 %. The remaining difference stems from a combination of misrepresenting the height of the aerosol layer (i.e. the DISAMAR-standard retrieval predicts decreased sensitivity to NO_2 starting higher up in the atmosphere), overestimated shielding by the effective cloud (i.e. scattering by aerosols in the DISAMAR-aerosol retrieval predicts more sensitivity within the aerosol layer), and a larger weighting of the cloudy component of the tropospheric AMF.

Several factors could lead to an O_2–O_2 effective cloud pressure that is smaller than the CALIOP effective aerosol layer pressure. Recall that the O_2–O_2 slant column is the proxy for effective cloud pressure in the O_2–O_2 cloud algorithm. This is based on the

Full Screen / Esc

Printer-friendly Version

Interactive Discussion

rationalization that a cloud has two main optical properties, transmission and reflection, and the O$_2$–O$_2$ slant column is a measure of the extent to which O$_2$–O$_2$ absorption below the cloud has been shielded. Thus, the light absorbing properties of aerosols are neglected in the O$_2$–O$_2$ retrieval Lambertian cloud model, and for strongly absorbing aerosols the reduced O$_2$–O$_2$ slant column will be interpreted as a smaller effective cloud pressure. For example, Fig. 12a and b shows simulations of the differential optical thickness at 465–485 nm of an aerosol layer with AOD equal to 1.5 and SSA equal 1.00 and 0.90, respectively. The layer is centered at 850 hPa and extends for 300 hPa, a typical aerosol vertical profile (see Fig. 3), and the surface albedo is 0.04 in both simulations. In each figure the differential optical thicknesses of Lambertian clouds with continuum reflectance equal to that of the aerosol layer simulation (i.e. equal cloud fraction) are shown for different cloud pressures.

Figure 12a shows that the differential optical thickness of the aerosol layer with SSA equal to 1.00 corresponds to a Lambertian cloud between 850 and 900 hPa. When the SSA decreases to 0.90, the differential optical thickness for the aerosol layer is reduced, and corresponds to a Lambertian cloud at 750 hPa (Fig. 12b).

Aerosol absorption would be enhanced if a strongly absorbing layer were elevated above a more optically thick scattering layer or equivalently if the surface albedo increased. This is shown in Fig. 12c, where the surface albedo for the simulation of an aerosol layer with AOD equal to 1.5 and SSA equal to 0.90 is increased from 0.04 to 0.07. The 477 nm differential optical thickness now corresponds to a Lambertian cloud at 650 hPa. Figure 13 shows the comparison of surface albedo and the difference between the observed effective cloud pressure and the observed effective aerosol layer pressure. The figure indeed indicates that negative differences between observed effective cloud pressure and observed effective aerosol layer pressure are associated with larger surface albedos, particularly when the AOD exceeds 0.7.

Another mechanism through which larger observed surface albedos could lead to lower effective cloud pressures is if the surface albedo climatology is biased high due to (1) cloud or smoke contamination (Kleipool et al., 2008), or (2) short-term darkening of

the surface by biomass burning. If a surface albedo larger than the actual scene albedo is used in the forward Lambertian cloud model, the expected O$_2$–O$_2$ slant columns would be too large (Fig. 12d), because the clear-sky contribution to the O$_2$–O$_2$ slant column would increase. The observed slant column would therefore be interpreted as a smaller effective cloud pressure.

Aerosol absorption also significantly affects the retrieved O$_2$–O$_2$ effective cloud fraction. Figure 14 shows that there is a strong correlation between the observed AOD and the observed effective cloud fraction. However, the slope of the linear fit between AOD and cloud fraction decreases with SSA. Cloud fractions for scattering aerosols (SSA > 0.95) are approximately 1.5–2 times larger than cloud fractions for absorbing aerosols. Thus, although scattering aerosols lead to larger retrieved effective cloud pressures, in the AMF calculation a larger weighting of the cloudy component of the tropospheric AMF will enhance shielding. Meanwhile, for absorbing aerosols, enhanced shielding in the AMF calculation due to smaller retrieved effective cloud pressures is offset by smaller effective cloud fractions. This highlights the compensating mechanisms at play behind the implicit aerosol correction in the current DOMINO NO$_2$ retrieval for scenes with high aerosol optical depth, and indicates the need for further investigation of the response of the O$_2$–O$_2$ effective cloud retrieval to aerosol contamination.

4   Discussion and conclusions

In this paper we analyzed the properties of the implicit aerosol correction in the DOMINO tropospheric NO$_2$ retrieval and presented an observation-based aerosol correction scheme using collocated OMI and CALIOP observations. We utilized three years of observations over South America, focusing on clear-sky pixels affected by biomass burning emissions. When all pixels were considered, tropospheric AMFs calculated with observed aerosol parameters were on average only 10 % higher than AMFs calculated with effective cloud parameters. Thus, errors in the implicit aerosol correction will be minimized in regional and seasonal averages of NO$_2$ tropospheric

columns. However, for individual pixels, when aerosol scattering and absorption is considered the tropospheric AMF can increase by as much as a factor of two compared to the implicit aerosol correction approach.

From our analysis we identified the ranges of retrieved O_2–O_2 effective cloud parameters where it is possible to distinguish pixels that have minimal errors from aerosol effects on the tropospheric AMF, as both the effective cloud fractions and the effective cloud pressures contain information about the aerosol concentration and vertical distribution. By filtering for effective cloud radiance fraction less than 0.3, or effective cloud pressure greater than 800 hPa, the difference between tropospheric AMFs based on implicit and explicit aerosol parameters is on average 6 and 3 %, respectively. These parameters fit the majority of the pixels considered in our study; 70 % had cloud radiance fraction below 30 %, and 50 % had effective cloud pressure greater than 800 hPa. We recommend using these ranges as a practical way to minimize aerosol related errors in version 2.0 of DOMINO NO_2 tropospheric columns when the presence of biomass burning aerosol emissions is expected. For validation experiments where aerosol interferences are likely, it may be possible to separate aerosol interference errors in the NO_2 tropospheric column from other retrieval algorithm errors by comparing observations under different cloud radiance fraction thresholds.

Retrievals with effective cloud pressure less than 800 hPa tend to have the largest differences in tropospheric AMF because typically these cloud pressures were lower than the collocated effective aerosol layer pressure observed by CALIOP. When observed aerosol parameters were included in the radiative transfer calculations, tropospheric AMFs were on average 20–40 % larger than the tropospheric AMFs derived using effective cloud parameters. These situations correspond with overestimated shielding in the implicit aerosol correction approach because the assumption of an opaque cloud underestimates the altitude resolved AMF below the effective cloud.

Simulations of O_2–O_2 differential optical thickness at 465–490 nm (the spectral window of the effective cloud retrieval) show that neglecting aerosol absorption in the Lambertian cloud model leads to lower retrieved effective cloud pressures as reduced

O_2–O_2 slant columns will be interpreted as a lower effective cloud pressures. This error was enhanced by higher surface albedos. Radiative transfer simulations of a typical aerosol layer showed that even lower effective cloud pressures could be retrieved if there is a high bias in the observed surface albedo monthly climatology. Sub-pixel cloud or aerosol contamination could lead to surface albedo errors. Particularly for pixels where active biomass burning is occurring, short-term darkening of the surface may not be captured in the monthly climatology because of the relatively coarse resolution of the dataset. Furthermore, outside of African savannas, most ecosystems do not burn every year, and after a burn the surface albedo recovers to pre-fire levels within 1–2 years (Gatebe et al., 2014). Thus, a higher spatial and temporal resolution surface albedo dataset may be necessary to retrieve reliable effective cloud parameters for scenes with active biomass burning.

Above an effective cloud fraction of 0.3 or an AOD of 0.60, tropospheric AMFs calculated with observed aerosol parameters were on average 30–50 % larger than the tropospheric AMFs derived using effective cloud parameters. These differences cannot be accounted for by the uncertainties in the retrieved aerosol parameters. This implies that for large fires or smoldering fires that release significant amounts of aerosols, the DOMINO NO₂ tropospheric columns may be significantly overestimated. In general, this has implications for the estimation of emissions from satellite NO₂ tropospheric column measurements for any source that is correlated with high aerosol concentrations, and suggests that current top-down emissions estimates could be overestimated.

In our analysis we compared AMFs from the DOMINO retrieval calculated by interpolating a look-up table with radiative transfer calculations from DISAMAR; the mean and SD of the difference was -0.6 ± 8 %. We also presented the first comparison of collocated AOD from the OMI near UV aerosol retrieval (OMAERUV) and CALIOP level 2 aerosol extinction vertical profile observations. We found good spatial correlation in the 3 year average ($R = 0.6$), and 72 % of the daily OMAERUV AOD observations were within 0.3 of the collocated CALIOP observations.

Our analysis holds promise for a strategy to include the effect of aerosols on tropospheric AMF calculations for clear sky pixels based on globally available satellite observations. Although, on average, the differences in tropospheric AMFs calculated with effective cloud parameters vs. observed aerosol parameters are small, tropospheric AMFs can differ by more than a factor of two. In order to include aerosol data in the retrieval, on line radiative transfer modeling would be required. Currently, this is computationally prohibitive for a near real-time retrieval. We suggest that for applications where spatial and temporal averaging is impossible, such as short-term validation campaigns, these effects should be considered.

Appendix A

In the OMAERUV retrieval pixels are labeled as cloud free if one of the following three conditions occurs: (1) when carbonaceous aerosol has been identified and the measured reflectivity at 388 nm is less than 0.16, (2) the difference between the measured scene reflectivity and the assumed surface albedo (ΔR) is less than or equal to 0.07, or (3) when carbonaceous aerosol has been identified and ΔR is less than or equal to 0.08 and the UV aerosol index (UVAI) is greater than or equal to 0.3.

The UVAI is a measure of the deviation of the observed UV spectral contrast from a pure Rayleigh scattering atmosphere. UVAI will be negative for scattering aerosols (Penning de Vries et al., 2009), positive for absorbing aerosols, and will increase with the height, the optical depth and the single scattering co-albedo of the absorbing aerosol layer (de Graaf, 2005; Torres et al., 1998).

Appendix B

The following sensitivity analysis shows how the uncertainties in the observed aerosol parameters used in the DISAMAR-aerosol tropospheric AMF calculations can account for only part of the 30–50 % average difference between the DISAMAR-standard and

DISAMAR-aerosol calculations for high AODs (> 0.6). Figures A1–A3 show the change in the DISAMAR-aerosol AMF when (a) the SSA is reduced by 0.05, the threshold for agreement for 75 % of OMAERUV SSA retrievals with AERONET observations, (b) the AOD is reduced by 30 % or 0.1 (whichever is greater), the estimated uncertainty of the OMAERUV AOD, and (c) the asymmetry parameter is reduced from 0.7 to 0.6, the approximate lower limit for the absorbing aerosol models used in the OMAERUV retrieval.

A 0.1 decrease in the asymmetry parameter resulted in an approximately 5 % (maximum 10 %) increase in AMF that is weakly correlated with AOD above AOD equal to ~ 0.5 (Fig. A1). At low optical thickness, the increase in AMF increases with AOD, consistent with an increase in the albedo effect from aerosols. The effect of reducing the AOD in the tropospheric AMF calculation depends on the effective ALH (Fig. A2), which to first order determines whether the aerosols shield NO_2 below, or enhance the light path and reflectance from within an aerosol-NO_2 mixed layer. For elevated aerosol layers (ALH > 3 km), the decrease in AOD resulted in a small decrease (< 5 %) or an increase (< 5 %) in AMF, consistent with a partial shielding aerosol effect. Regardless of ALH, when the AOD exceeds 2, aerosols are predominantly shielding, and a decrease in the AOD results in a 0–10 % increase in AMF. When the aerosol extinction profile has an effective ALH less than 2 km, a decrease in the AOD results in at most a 20 % decrease in AMF, but on average a 5–10 % decrease, indicating a predominantly albedo aerosol affect.

For large (> 0.6) optical depths, the uncertainty in the SSA contributes the most to uncertainties in the DISAMAR-aerosol AMF calculation (Fig. A3). In general, the DISAMAR-aerosol AMF decreased when the SSA was reduced by 0.05, as increased light absorption by aerosols reduces the sensitivity to NO_2. The sensitivity of the AMF calculation to the uncertainty in SSA increased with AOD; the AMF decreased by at most ~ 15 % for AOD greater than 1.

The Supplement related to this article is available online at doi:10.5194/amtd-8-2683-2015-supplement.

Title Page

Abstract | Introduction

Conclusions | References

Tables | Figures

|◄ | ►|

◄ | ►

Back | Close

Full Screen / Esc

Printer-friendly Version

Interactive Discussion

References

Acarreta, J. R., de Haan, J. F., and Stammes, P.: Cloud pressure retrieval using the O_2–O_2 absorption band at 477 nm, J. Geophys. Res., 109, D05204, doi:10.1029/2003JD003915, 2004.

Ahn, C., Torres, O., and Jethva, H.: Assessment of OMI near UV aerosol optical depth over land, J. Geophys. Res. Atmos., 119, 2457–2473, 2014.

Beirle, S., Boersma, K. F., Platt, U., Lawrence, M. G., and Wagner, T.: Megacity Emissions and Lifetimes of Nitrogen Oxides Probed from Space, Science, 333, 1737–1739, doi:10.1126/science.1207824, 2011.

Boersma, K. F., Eskes, H. J., and Brinksma, E. J.: Error analysis for tropospheric NO_2 retrieval from space, J. Geophys. Res., 109, D04311, doi:10.1029/2003JD003962, 2004.

Boersma, K. F., Eskes, H. J., Dirksen, R. J., van der A, R. J., Veefkind, J. P., Stammes, P., Huijnen, V., Kleipool, Q. L., Sneep, M., Claas, J., Leitão, J., Richter, A., Zhou, Y., and Brunner, D.: An improved tropospheric NO_2 column retrieval algorithm for the Ozone Monitoring Instrument, Atmos. Meas. Tech., 4, 1905–1928, doi:10.5194/amt-4-1905-2011, 2011.

Braak, R.: Row Anomaly Flagging Rules Lookup Table, KNMI, De Bilt, 2010.

Bucsela, E. J., Pickering, K. E., Huntemann, T. L., Cohen, R. C., Perring, A., Gleason, J. F., Blakeslee, R. J., Albrecht, R. I., Holzworth, R., Cipriani, J. P., Vargas-Navarro, D., Mora-Segura, I., Pacheco-Hernández, A., and Laporte-Molina, S.: Lightning-generated NO_x seen by the Ozone Monitoring Instrument during NASA's Tropical Composition, Cloud and Climate Coupling Experiment (TC 4), J. Geophys. Res., 115, D00J10, doi:10.1029/2009JD013118, 2010.

Title Page

Abstract | Introduction

Conclusions | References

Tables | Figures

|◄ | ►|

◄ | ►

Back | Close

Full Screen / Esc

Printer-friendly Version

Interactive Discussion

Castellanos, P. and Boersma, K. F.: Reductions in nitrogen oxides over Europe driven by environmental policy and economic recession, Sci. Rep., 2, 265, doi:10.1038/srep00265, 2012.

Castellanos, P., Boersma, K. F., and van der Werf, G. R.: Satellite observations indicate substantial spatiotemporal variability in biomass burning NO_x emission factors for South America, Atmos. Chem. Phys., 14, 3929–3943, doi:10.5194/acp-14-3929-2014, 2014.

Caudill, T. R., Flittner, D. E., Herman, B. M., Torres, O., and McPeters, R. D.: Evaluation of the pseudo-spherical approximation for backscattered ultraviolet radiances and ozone retrieval, J. Geophys. Res., 102, 3881, doi:10.1029/96JD03266, 1997.

de Graaf, M.: Absorbing Aerosol Index: sensitivity analysis, application to GOME and comparison with TOMS, J. Geophys. Res., 110, D01201, doi:10.1029/2004JD005178, 2005.

de Haan, J. F.: DISAMAR Algorithm description and background information, Royal Netherlands Meteoroligical Institute, De Bilt, the Netherlands, 2011.

de Haan, J. F., Bosma, P. B., and Hovenier, J. W.: The adding method for multiple scattering calculations of polarized light, Astron. Astrophys., 183, 371–391, 1987.

de Ruyter de Wildt, M., Eskes, H., and Boersma, K. F.: The global economic cycle and satellite-derived NO_2 trends over shipping lanes, Geophys. Res. Lett., 39, L01802, doi:10.1029/2011GL049541, 2012.

Dirksen, R. J., Boersma, K. F., Eskes, H. J., Ionov, D. V., Bucsela, E. J., Levelt, P. F., and Kelder, H. M.: Evaluation of stratospheric NO_2 retrieved from the Ozone Monitoring Instrument: intercomparison, diurnal cycle, and trending, J. Geophys. Res., 116, D08305, doi:10.1029/2010JD014943, 2011.

Dubovik, O., Holben, B., Eck, T. F., Smirnov, A., Kaufman, Y. J., King, M. D., Tanré, D., and Slutsker, I.: Variability of absorption and optical properties of key aerosol types observed in worldwide locations, J. Atmos. Sci., 59, 590–608, 2002.

Eskes, H. J. and Boersma, K. F.: Averaging kernels for DOAS total-column satellite retrievals, Atmos. Chem. Phys., 3, 1285–1291, doi:10.5194/acp-3-1285-2003, 2003.

Gatebe, C. K., Ichoku, C. M., Poudyal, R., Roman, M. O., and Wilcox, E.: Surface albedo darkening from wildfires in northern sub-Saharan Africa, Environ. Res. Lett., 9, 065003, doi:10.1088/1748-9326/9/6/065003, 2014.

Holben, B. N., Eck, T. F., Slutsker, I., Tanré, D., Buis, J. P., Setzer, A., Vermote, E., Reagan, J. A., Kaufman, Y. J., Nakajima, T., Lavenu, F., Jankowiak, I., and Smirnov, A.: AERONET – a federated instrument network and data archive for aerosol characterization, Remote Sens. Environ., 66, 1–16, doi:10.1016/S0034-4257(98)00031-5, 1998.

OMI tropospheric NO_2 air mass factors over South America

P. Castellanos et al.

Title Page

Abstract	Introduction
Conclusions	References
Tables	Figures

Back | Close

Full Screen / Esc

Printer-friendly Version

Interactive Discussion

Irie, H., Boersma, K. F., Kanaya, Y., Takashima, H., Pan, X., and Wang, Z. F.: Quantitative bias estimates for tropospheric NO_2 columns retrieved from SCIAMACHY, OMI, and GOME-2 using a common standard for East Asia, Atmos. Meas. Tech., 5, 2403–2411, doi:10.5194/amt-5-2403-2012, 2012.

5   Jaeglé, L., Steinberger, L., Martin, R. V., and Chance, K.: Global partitioning of NO_x sources using satellite observations: relative roles of fossil fuel combustion, biomass burning and soil emissions, Faraday Discuss., 130, 407–423, doi:10.1039/B502128F, 2005.

Kim, S.-W., Berthier, S., Raut, J.-C., Chazette, P., Dulac, F., and Yoon, S.-C.: Validation of aerosol and cloud layer structures from the space-borne lidar CALIOP using a ground-based

10   lidar in Seoul, Korea, Atmos. Chem. Phys., 8, 3705–3720, doi:10.5194/acp-8-3705-2008, 2008.

Kleipool, Q. L., Dobber, M. R., de Haan, J. F., and Levelt, P. F.: Earth surface reflectance climatology from 3 years of OMI data, J. Geophys. Res., 113, D18308, doi:10.1029/2008JD010290, 2008.

15   Koelemeijer, R. B. A. and Stammes, P.: Effects of clouds on ozone column retrieval from GOME UV measurements, J. Geophys. Res., 104, 8281, doi:10.1029/1999JD900012, 1999.

Leitão, J., Richter, A., Vrekoussis, M., Kokhanovsky, A., Zhang, Q. J., Beekmann, M., and Burrows, J. P.: On the improvement of NO_2 satellite retrievals – aerosol impact on the airmass factors, Atmos. Meas. Tech., 3, 475–493, doi:10.5194/amt-3-475-2010, 2010.

20   Levelt, P. F., van den Oord, G. H. J., Dobber, M. R., Malkki, A., Visser, H., de Vries, J., Stammes, P., Lundell, J. O. V., and Saari, H.: The ozone monitoring instrument, IEEE T. Geosci. Remote, 44, 1093–1101, doi:10.1109/TGRS.2006.872333, 2006.

Lin, J.-T., Martin, R. V., Boersma, K. F., Sneep, M., Stammes, P., Spurr, R., Wang, P., Van Roozendael, M., Clémer, K., and Irie, H.: Retrieving tropospheric nitrogen dioxide from

25   the Ozone Monitoring Instrument: effects of aerosols, surface reflectance anisotropy, and vertical profile of nitrogen dioxide, Atmos. Chem. Phys., 14, 1441–1461, doi:10.5194/acp-14-1441-2014, 2014.

Liu, Z., Vaughan, M., Winker, D., Kittaka, C., Getzewich, B., Kuehn, R., Omar, A., Powell, K., Trepte, C., and Hostetler, C.: The CALIPSO lidar cloud and aerosol discrimination: version

30   2 algorithm and initial assessment of performance, J. Atmos. Ocean. Tech., 26, 1198–1213, doi:10.1175/2009JTECHA1229.1, 2009.

Ma, J. Z., Beirle, S., Jin, J. L., Shaiganfar, R., Yan, P., and Wagner, T.: Tropospheric NO_2 vertical column densities over Beijing: results of the first three years of ground-based MAX-DOAS

Title Page

Abstract | Introduction

Conclusions | References

Tables | Figures

|◄ | ►|

◄ | ►

Back | Close

Full Screen / Esc

Printer-friendly Version

Interactive Discussion

measurements (2008–2011) and satellite validation, Atmos. Chem. Phys., 13, 1547–1567, doi:10.5194/acp-13-1547-2013, 2013.

Maasakkers, J. D.: Vital improvements to the retrieval of tropospheric NO_2 columns from the Ozone Monitoring Instrument, Eindhoven University of Technology, Eindhoven, July 2013.

Marais, E. A., Jacob, D. J., Kurosu, T. P., Chance, K., Murphy, J. G., Reeves, C., Mills, G., Casadio, S., Millet, D. B., Barkley, M. P., Paulot, F., and Mao, J.: Isoprene emissions in Africa inferred from OMI observations of formaldehyde columns, Atmos. Chem. Phys., 12, 6219–6235, doi:10.5194/acp-12-6219-2012, 2012.

Martin, R. V.: An improved retrieval of tropospheric nitrogen dioxide from GOME, J. Geophys. Res., 107, 4437, doi:10.1029/2001JD001027, 2002.

Mebust, A. K., Russell, A. R., Hudman, R. C., Valin, L. C., and Cohen, R. C.: Characterization of wildfire NO_x emissions using MODIS fire radiative power and OMI tropospheric NO_2 columns, Atmos. Chem. Phys., 11, 5839–5851, doi:10.5194/acp-11-5839-2011, 2011.

Omar, A. H., Winker, D. M., Vaughan, M. A., Hu, Y., Trepte, C. R., Ferrare, R. A., Lee, K.-P., Hostetler, C. A., Kittaka, C., Rogers, R. R., Kuehn, R. E., and Liu, Z.: The CALIPSO Automated Aerosol Classification and Lidar Ratio Selection Algorithm, J. Atmos. Ocean. Tech., 26, 1994–2014, doi:10.1175/2009JTECHA1231.1, 2009.

Palmer, P. I., Jacob, D. J., Chance, K., Martin, R. V., Spurr, R. J. D., Kurosu, T. P., Bey, I., Yantosca, R., Fiore, A., and Li, Q.: Air mass factor formulation for spectroscopic measurements from satellites: application to formaldehyde retrievals from the Global Ozone Monitoring Experiment, J. Geophys. Res., 106, 14539, doi:10.1029/2000JD900772, 2001.

Penning de Vries, M. J. M., Beirle, S., and Wagner, T.: UV Aerosol Indices from SCIA-MACHY: introducing the SCattering Index (SCI), Atmos. Chem. Phys., 9, 9555–9567, doi:10.5194/acp-9-9555-2009, 2009.

Schreier, S. F., Richter, A., Schepaschenko, D., Shvidenko, A., Hilboll, A., and Burrows, J. P.: Differences in satellite-derived NOx emission factors between Eurasian and North American boreal forest fires, Atmos. Environ., doi:10.1016/j.atmosenv.2014.08.071, in press, 2014.

Sneep, M., de Haan, J. F., Stammes, P., Wang, P., Vanbauce, C., Joiner, J., Vasilkov, A. P., and Levelt, P. F.: Three-way comparison between OMI and PARASOL cloud pressure products, J. Geophys. Res., 113, D15S23, doi:10.1029/2007JD008694, 2008.

Stammes, P., Sneep, M., de Haan, J. F., Veefkind, J. P., Wang, P., and Levelt, P. F.: Effective cloud fractions from the Ozone Monitoring Instrument: theoretical framework and validation, J. Geophys. Res., 113, D16S38, doi:10.1029/2007JD008820, 2008.

Stavrakou, T., Müller, J.-F., Boersma, K. F., van der A, R. J., Kurokawa, J., Ohara, T., and Zhang, Q.: Key chemical NO_x sink uncertainties and how they influence top-down emissions of nitrogen oxides, Atmos. Chem. Phys., 13, 9057–9082, doi:10.5194/acp-13-9057-2013, 2013.

5 Torres, O., Bhartia, P. K., Herman, J. R., Ahmad, Z., and Gleason, J.: Derivation of aerosol properties from satellite measurements of backscattered ultraviolet radiation: theoretical basis, J. Geophys. Res., 103, 17099, doi:10.1029/98JD00900, 1998.

Torres, O., Tanskanen, A., Veihelmann, B., Ahn, C., Braak, R., Bhartia, P. K., Veefkind, P., and Levelt, P.: Aerosols and surface UV products from Ozone Monitoring Instrument observa-
10 tions: an overview, J. Geophys. Res., 112, D24S47, doi:10.1029/2007JD008809, 2007.

Torres, O., Ahn, C., and Chen, Z.: Improvements to the OMI near-UV aerosol algorithm using A-train CALIOP and AIRS observations, Atmos. Meas. Tech., 6, 3257–3270, doi:10.5194/amt-6-3257-2013, 2013.

van der Werf, G. R., Randerson, J. T., Giglio, L., Collatz, G. J., Mu, M., Kasibhatla, P. S., Mor-
15 ton, D. C., DeFries, R. S., Jin, Y., and van Leeuwen, T. T.: Global fire emissions and the contribution of deforestation, savanna, forest, agricultural, and peat fires (1997–2009), Atmos. Chem. Phys., 10, 11707–11735, doi:10.5194/acp-10-11707-2010, 2010.

Vandaele, A. C., Hermans, C., Simon, P. C., Carleer, M., Colin, R., Fally, S., Mérienne, M. F., Jenouvrier, A., and Coquart, B.: Measurements of the NO2 absorption cross-section from
20 $42000\,cm^{-1}$ to $10000\,cm^{-1}$ (238–1000 nm) at 220 and 294 K, J. Quant. Spectrosc. Ra., 59, 171–184, doi:10.1016/S0022-4073(97)00168-4, 1998.

van Geffen, J. H. G. M., Boersma, K. F., Van Roozendael, M., Hendrick, F., Mahieu, E., De Smedt, I., Sneep, M., and Veefkind, J. P.: Improved spectral fitting of nitrogen dioxide from OMI in the 405–465 nm window, Atmos. Meas. Tech. Discuss., 7, 10619–10671,
25 doi:10.5194/amtd-7-10619-2014, 2014.

Vaughan, M. A., Powell, K. A., Winker, D. M., Hostetler, C. A., Kuehn, R. E., Hunt, W. H., Getzewich, B. J., Young, S. A., Liu, Z., and McGill, M. J.: Fully automated detection of cloud and aerosol layers in the CALIPSO lidar measurements, J. Atmos. Ocean. Tech., 26, 2034–2050, doi:10.1175/2009JTECHA1228.1, 2009.

30 Vinken, G. C. M., Boersma, K. F., van Donkelaar, A., and Zhang, L.: Constraints on ship NO_x emissions in Europe using GEOS-Chem and OMI satellite NO_2 observations, Atmos. Chem. Phys., 14, 1353–1369, doi:10.5194/acp-14-1353-2014, 2014.

**OMI tropospheric
NO_2 air mass factors
over South America**

P. Castellanos et al.

Title Page

Abstract	Introduction
Conclusions	References
Tables	Figures

|◄ | ►|

◄ | ►

Back | Close

Full Screen / Esc

Printer-friendly Version

Interactive Discussion

Winker, D. M., Pelon, J., Coakley Jr., J. A., Ackerman, S. A., Charlson, R. J., Colarco, P. R., Flamant, P., Fu, Q., Hoff, R. M., Kittaka, C., Kubar, T. L., Le Treut, H., McCormick, M. P., Mégie, G., Poole, L., Powell, K., Trepte, C., Vaughan, M. A., and Wielicki, B. A.: The CALIPSO Mission: a global 3D view of aerosols and clouds, B. Am. Meteorol. Soc., 91, 1211–1229, doi:10.1175/2010BAMS3009.1, 2010.

Winker, D. M., Tackett, J. L., Getzewich, B. J., Liu, Z., Vaughan, M. A., and Rogers, R. R.: The global 3-D distribution of tropospheric aerosols as characterized by CALIOP, Atmos. Chem. Phys., 13, 3345–3361, doi:10.5194/acp-13-3345-2013, 2013.

Young, S. A. and Vaughan, M. A.: The retrieval of profiles of particulate extinction from cloud-aerosol lidar infrared pathfinder satellite observations (CALIPSO) data: algorithm description, J. Atmos. Ocean. Tech., 26, 1105–1119, doi:10.1175/2008JTECHA1221.1, 2009.

OMI tropospheric NO$_2$ air mass factors over South America

P. Castellanos et al.

Title Page

Abstract	Introduction
Conclusions	References
Tables	Figures

|◄   ►|

◄   ►

Back   Close

Full Screen / Esc

Printer-friendly Version

Interactive Discussion

Table 1. Ranges of parameters that are observed by OMI for which less than 20 % biomass burning aerosol-related average error in the AMF can be expected.

Expected Average AMF Error	Effective Cloud Radiance Fraction	Effective Cloud Pressure	Aerosol Optical Depth
< 20 %	< 30 %	> 800 hPa	< 0.6
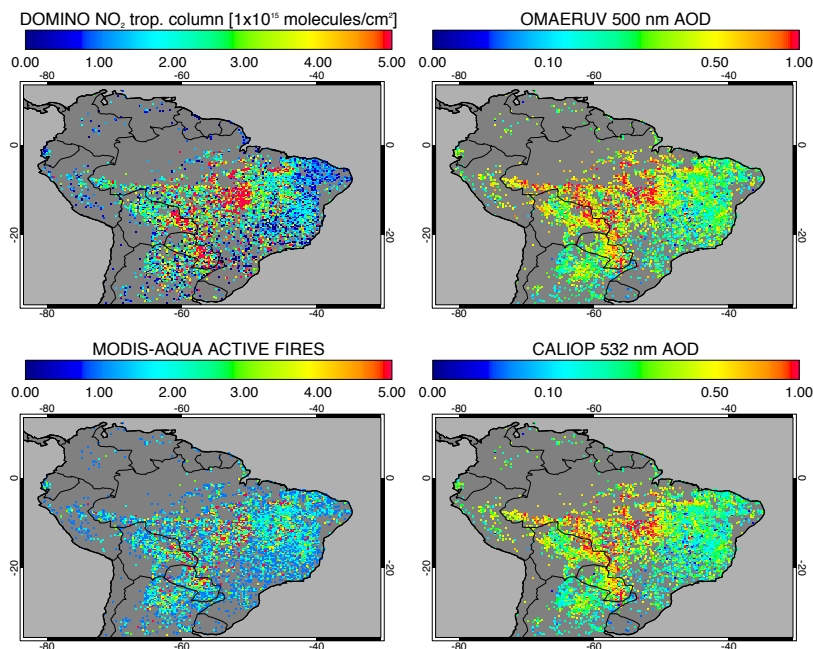
Figure 1. The 2006–2008 fire season (July–November) average DOMINO v2 NO2 tropospheric columns, OMAERUV 500 nm AOD, MODIS-Aqua active fires, and CALIOP lv2 532 nm AOD. Pixels were selected and re-gridded to 0.25° × 0.25° if all of the following conditions were met: 1) MODIS-aqua detected an active fire with at least 80 % confidence, 2) the DOMINO v2 retrieval reported tropospheric column flag equal to zero, 3) and the OMAERUV retrieval reported algorithm quality flag equal to zero. CALIOP lv2 pixels were collocated with OMI pixels by averaging together all daytime CALIOP extinction vertical profiles within 0.5° of the OMI pixel center. For the AOD calculation we selected aerosol layers where the cloud-aerosol discrimination (CAD) score was less than −20, the QC-flag was equal to 0 or 1, and the extinction uncertainty was less than 99.9.
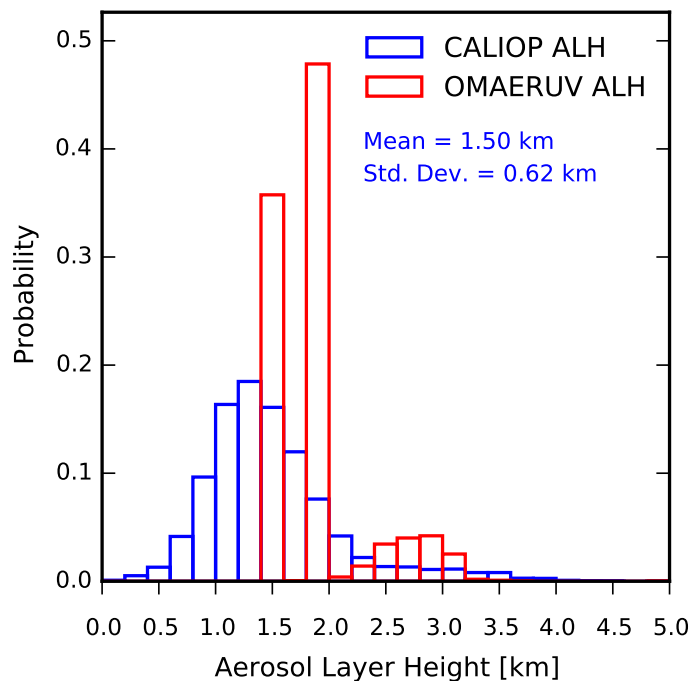
Figure 2. The probability distributions of the prescribed aerosol layer height (ALH) in the OMAERUV retrieval, and the effective ALH (Eq. 7) derived from CALIOP 532 nm observed aerosol extinction vertical profiles.
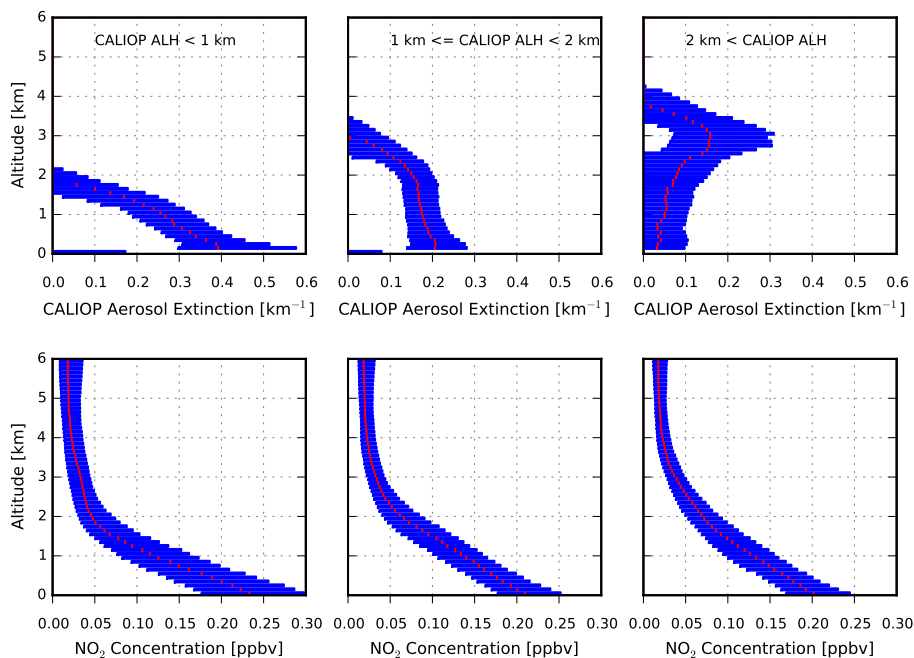
Figure 3. The shape of the observed CALIOP aerosol extinction vertical profile and the collocated simulated TM4 NO$_2$ profile for three ranges of CALIOP effective ALH: less than 1 km, 1–2 km, and greater than 2 km. This plot was made by scaling all extinction vertical profiles to an AOD of 0.5 and NO$_2$ profiles to a tropospheric vertical column equal to 1 before averaging by layer. The red dots indicate the average in each layer, and the extent of the blue boxes represents the first and third quartiles in each layer.
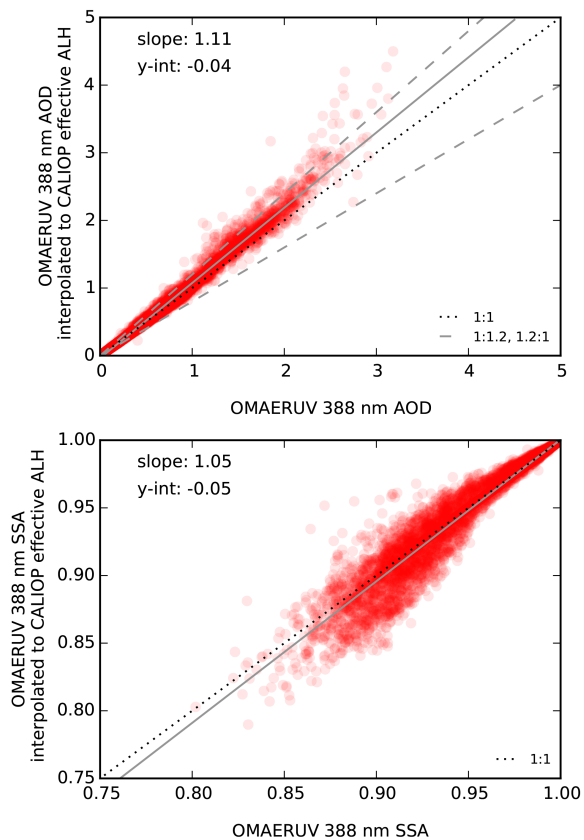
Figure 4. The change in the OMAERUV 388 nm AOD and SSA from replacing the standard retrieval prescribed aerosol layer height (ALH) with the CALIOP observed effective ALH.
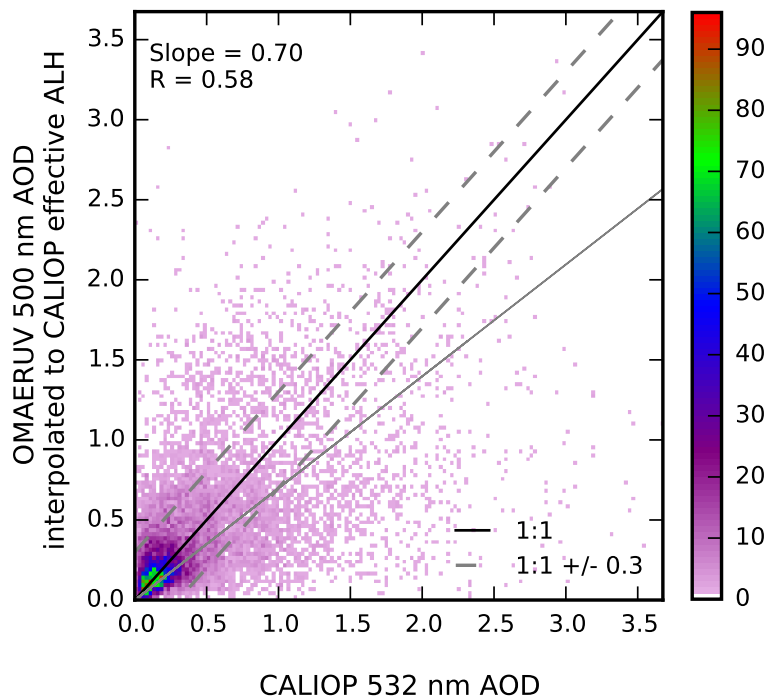
Figure 5. Comparison of daily OMAERUV 500 nm AOD and collocated CALIOP lv2 532 nm AOD for the 2006–2008 fire season (July–November) over South America. The gray dashed line represents the least squares fit through the origin. See Fig. 1 for the pixel and layer selection criteria.

Title Page

Abstract | Introduction

Conclusions | References

Tables | Figures

|◄ | ►|

◄ | ►

Back | Close

Full Screen / Esc

Printer-friendly Version

Interactive Discussion
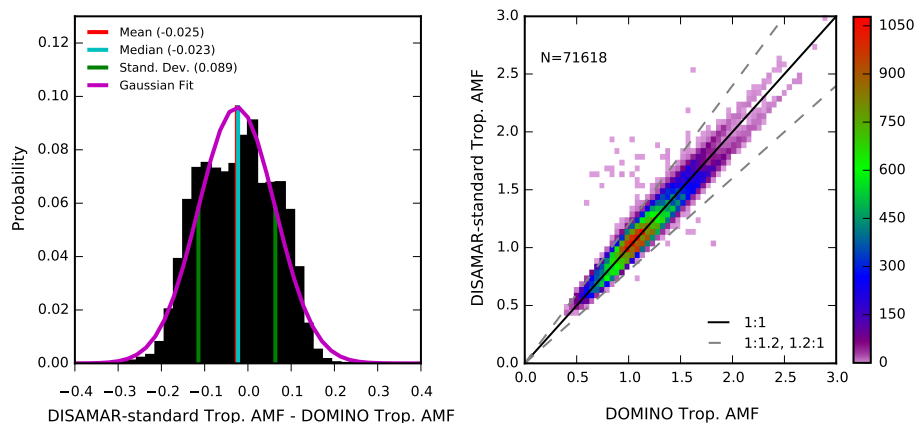
Figure 6. The probability distribution of the differences in AMF retrieved by DISAMAR and DOMINO for all pixels in which MODIS-Aqua reported an active fire between July and November in 2006–2008. The DOMINO tropospheric AMF data was filtered for tropospheric quality flag equal to zero and surface albedo less than 0.3.
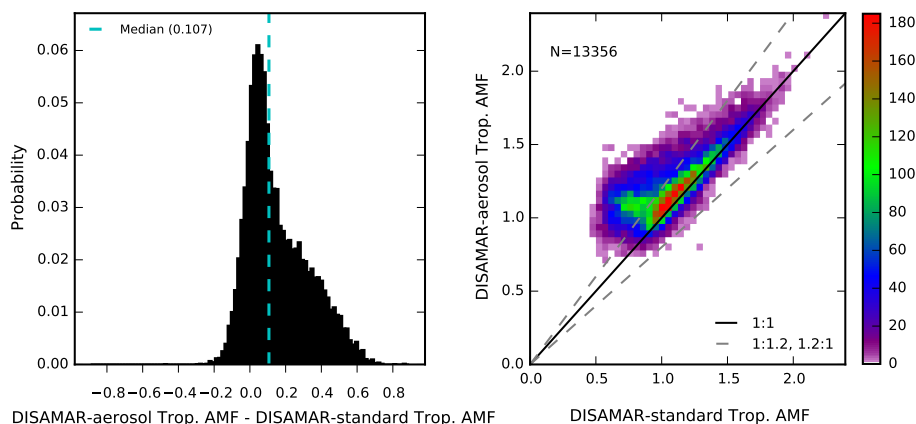
Figure 7. Comparison between DISAMAR tropospheric AMFs calculated with the standard retrieval using parameters from DOMINO v2.0 (DISAMAR-standard), and DISAMAR tropospheric AMFS calculated with explicit aerosol effects (DISAMAR-aerosol). The AOD and SSA for these retrievals are determined by the OMAERUV retrieval, and aerosol extinction profiles were taken from the CALIOP lv2 retrieval.
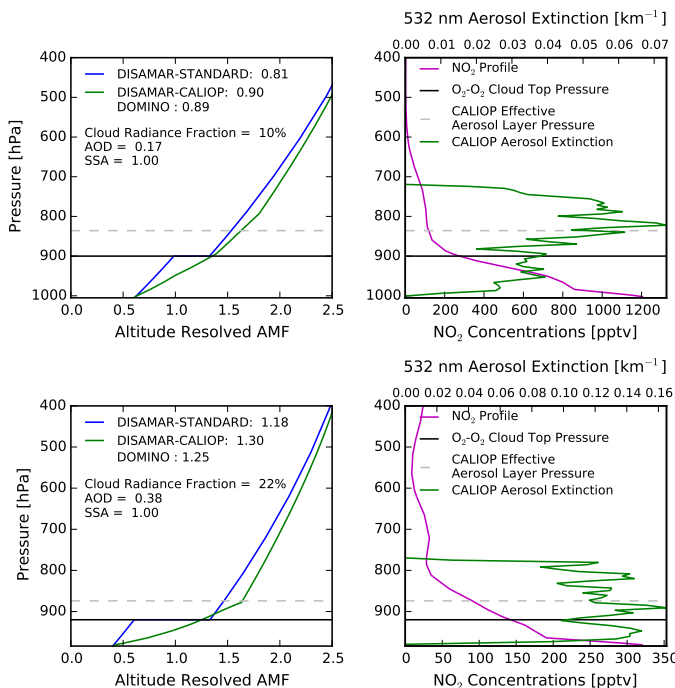
Figure 8. On the left are altitude resolved AMFs from the DISAMAR-standard and DISAMAR-aerosol calculations. The tropospheric AMF is given next to each label in the legend, and the DOMINO tropospheric AMF is given for reference. On the right are the NO$_2$ profiles from the TM4 simulations that are used in the retrievals, along with the CALIOP lv2 aerosol extinction profiles utilized in the DISMAR-aerosol calculations. In all the plots, the O$_2$–O$_2$ retrieved effective cloud top pressure is shown as a horizontal black line, and the CALIOP effective aerosol layer pressure is shown as a dashed horizontal gray line. For this figure we show the results for typical retrievals where the difference between the DISAMAR-standard and DISAMAR-aerosol tropospheric AMFs are less than ±0.2.
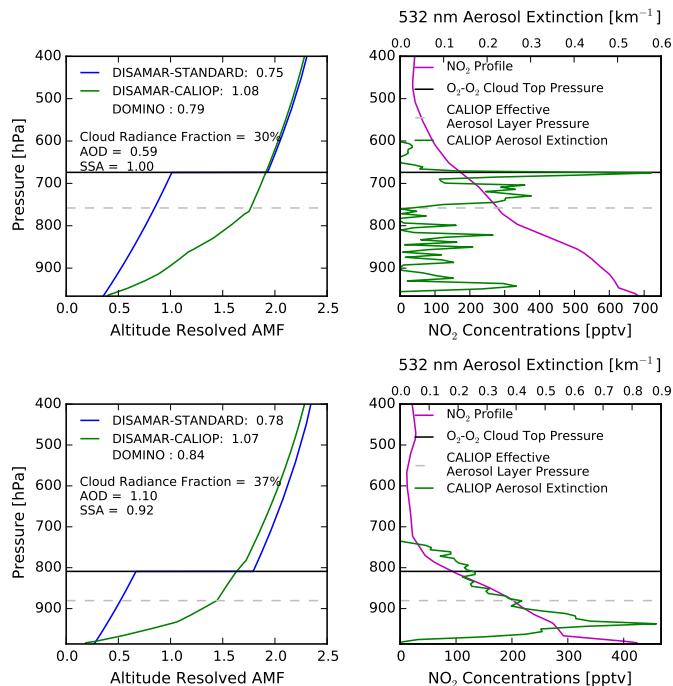
Figure 9. On the left are altitude resolved AMFs from the DISAMAR-standard and DISAMAR-aerosol calculations. The tropospheric AMF is given next to each label in the legend, and the DOMINO tropospheric AMF is given for reference. On the right are the NO_2 profiles from the TM4 simulations that are used in the retrievals, along with the CALIOP lv2 aerosol extinction profiles utilized in the DISMAR-aerosol calculations. In all the plots, the O_2–O_2 retrieved effective cloud top pressure is shown as a horizontal black line, and the CALIOP effective aerosol layer pressure is shown as a dashed horizontal gray line. For this figure we show the results for two typical retrievals where the difference between the DISAMAR-standard and DISAMAR-aerosol tropospheric AMFs are greater than 0.2.

OMI tropospheric NO₂ air mass factors over South America

P. Castellanos et al.

Title Page

Abstract | Introduction

Conclusions | References

Tables | Figures

|◀ | ▶|

◀ | ▶

Back | Close

Full Screen / Esc

Printer-friendly Version

Interactive Discussion
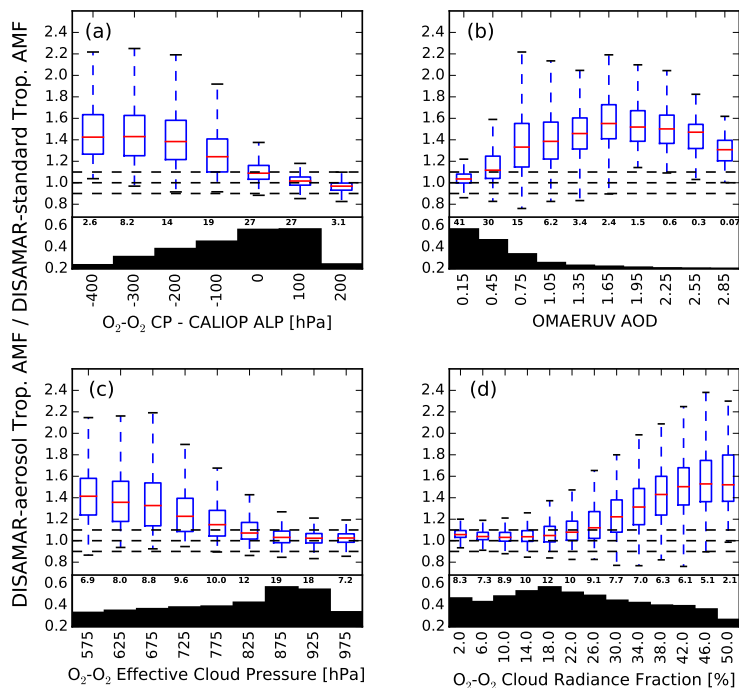
Figure 10. The ratio of the DISAMAR-aerosol tropospheric AMF to the DISAMAR-standard tropospheric AMF with respect to **(a)** the difference in the CALIOP effective aerosol layer pressure (ALP) and the O_2–O_2 effective cloud top pressure, **(b)** the OMAERUV AOD, **(c)** the O_2–O_2 effective cloud top pressure, and **(d)** the O_2–O_2 cloud radiance fraction. The red lines represent the mean for each bin. The extent of the blue boxes represents the first and third quartiles for each bin. Finally, the whiskers represent three SDs for each bin. The black boxes and numbers at the bottom of each plot are the fractions in percent of the total number of pixels that fall in each bin.
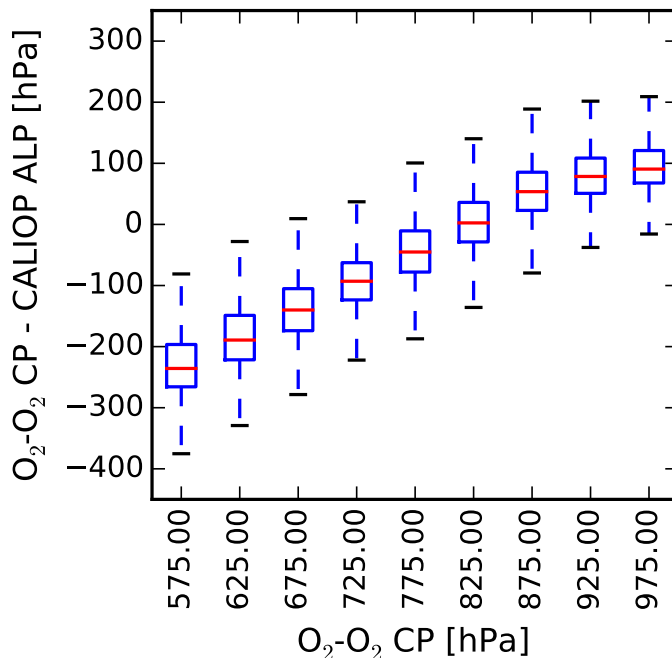
Figure 11. The difference in the CALIOP effective aerosol layer pressure (ALP) and the O_2–O_2 effective cloud top pressure with respect to the O_2–O_2 effective cloud top pressure. The red lines represent the mean for each bin. The extent of the blue boxes represents the first and third quartiles for each bin. The whiskers represent three SDs for each bin.
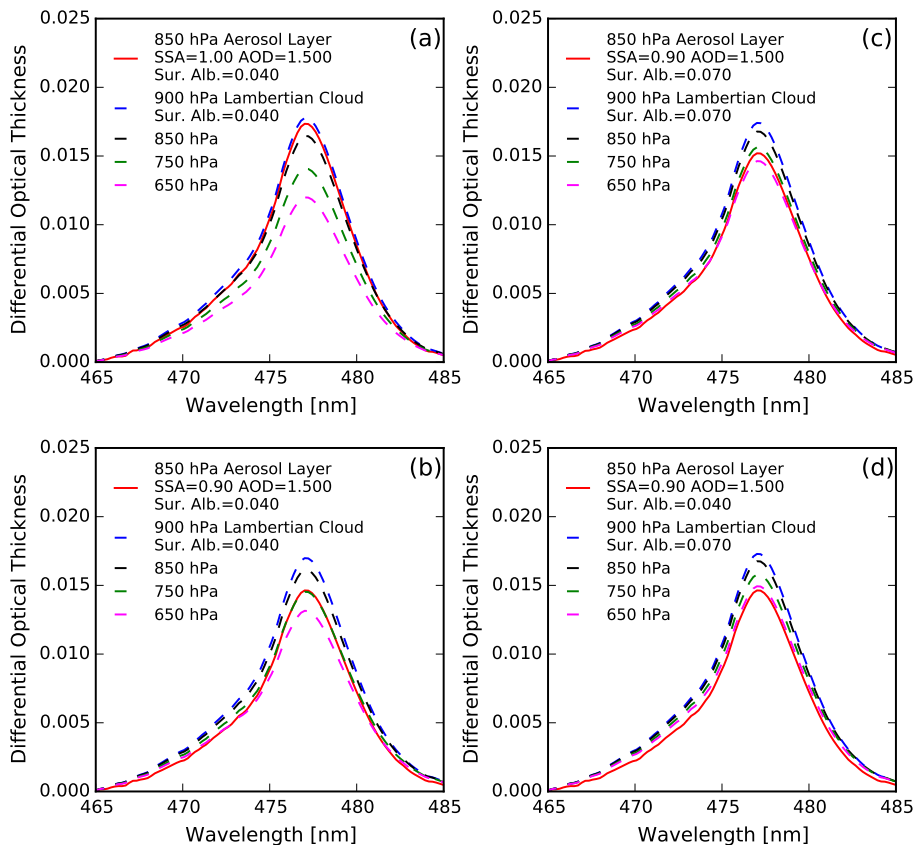
Figure 12. Simulations of differential optical thickness for an aerosol layer centered at 850 hPa and extending for 300 hPa. In each figure the differential optical thicknesses of Lambertian clouds with continuum reflectance equal to that of the aerosol layer simulation (i.e. equal cloud fraction) are shown for different cloud pressures.

Title Page

Abstract | Introduction

Conclusions | References

Tables | Figures

Back | Close

Full Screen / Esc

Printer-friendly Version

Interactive Discussion
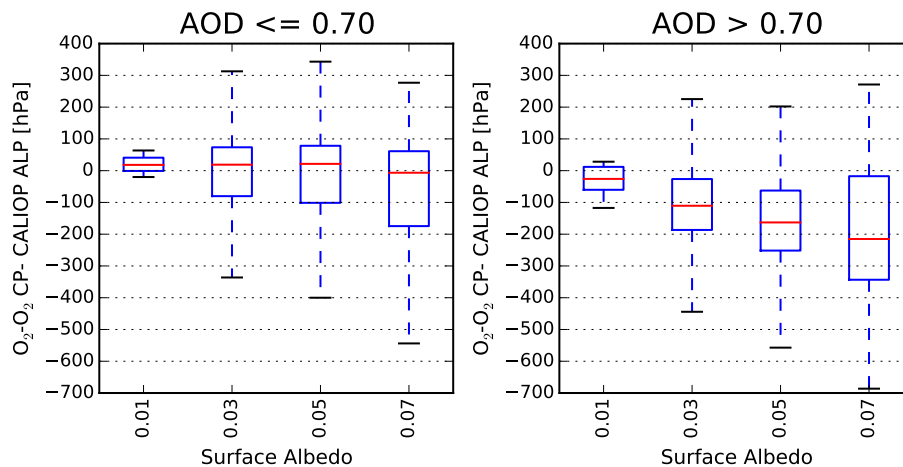
Figure 13. Comparison of the surface albedo utilized in the O$_2$–O$_2$ retrieval with the difference between the O$_2$–O$_2$ effective cloud pressure and the CALIOP observed effective aerosol layer pressure.

Discussion Paper | Discussion Paper | Discussion Paper | Discussion Paper

AMTD

8, 2683–2733, 2015

OMI tropospheric NO$_2$ air mass factors over South America

P. Castellanos et al.

Title Page

Abstract | Introduction
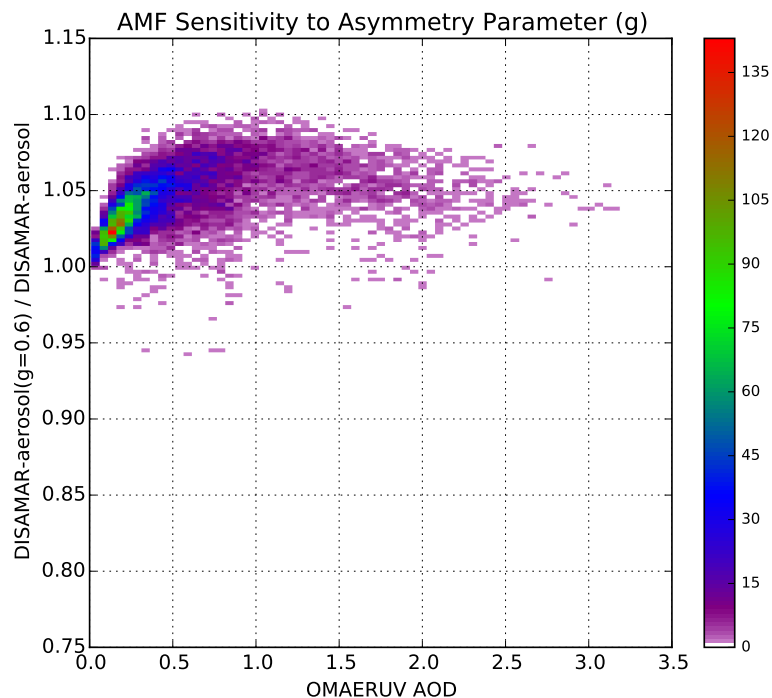
Conclusions | References

Tables | Figures

|◀ | ▶|

◀ | ▶

Back | Close

Full Screen / Esc

Printer-friendly Version

Interactive Discussion
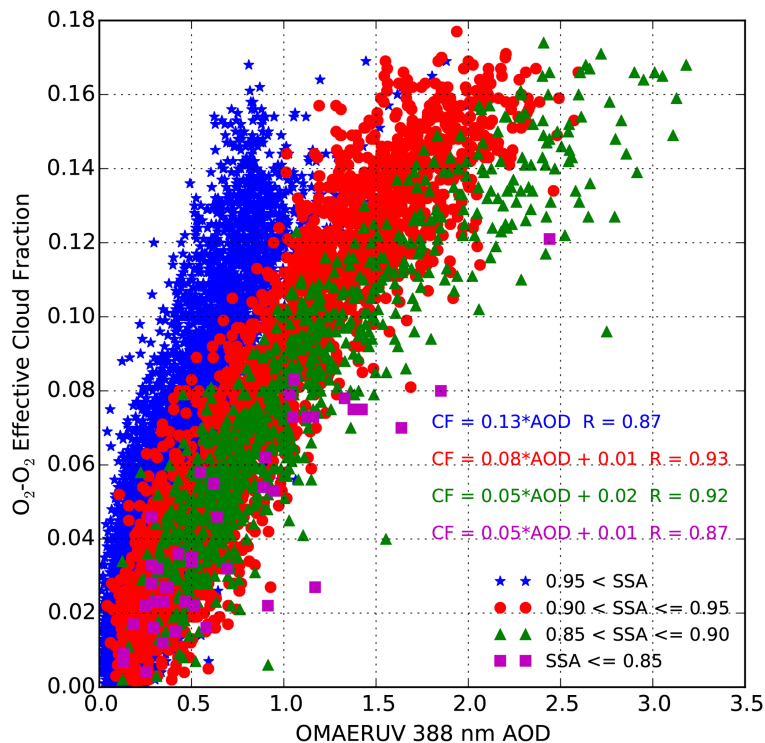
Figure 14. Comparison of the OMAERUV retrieved 388 nm AOD and observed effective cloud fraction binned by the OMAERUV retrieved SSA.

Figure A1. The change in the calculated tropospheric AMF as a result of a decrease from 0.7 to 0.6 in the aerosol asymmetry parameter (g) used in the DISAMAR radiative transfer model.

Title Page

Abstract | Introduction

Conclusions | References

Tables | Figures

|◀ | ▶|

◀ | ▶

Back | Close

Full Screen / Esc

Printer-friendly Version

Interactive Discussion
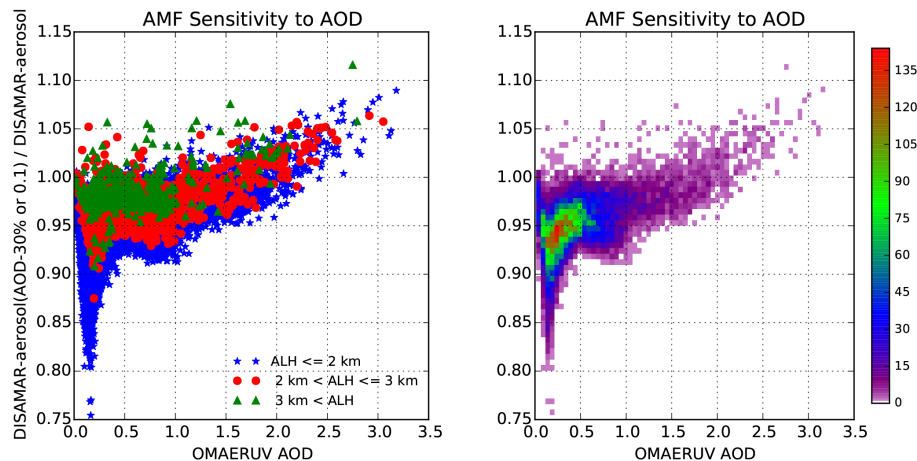
Figure A2. The change in the calculated tropospheric AMF as a result of a 30 % or 0.1 decrease (whichever is larger) in the AOD used in the DISAMAR radiative transfer model.
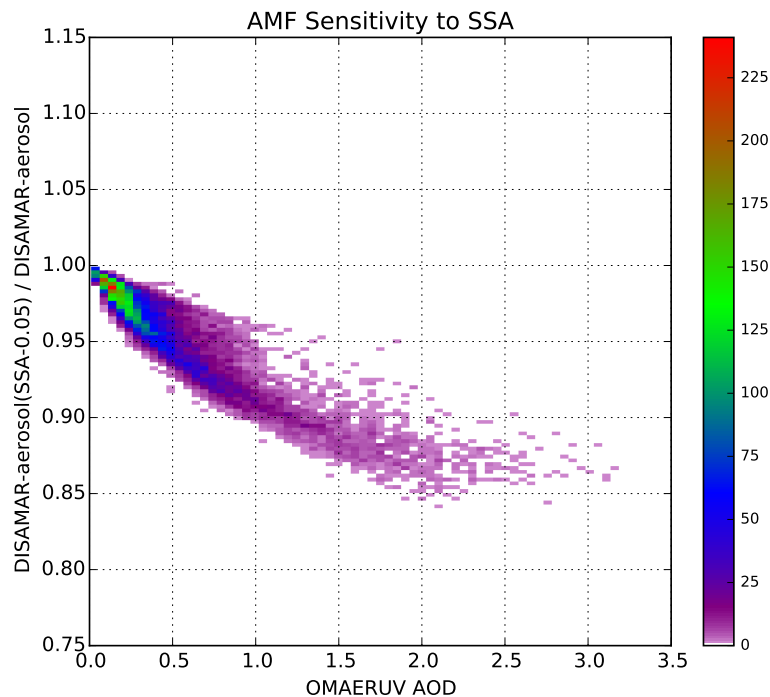
Full Screen / Esc

Printer-friendly Version

Interactive Discussion

Figure A3. The change in the calculated tropospheric AMF as a result of a 0.05 decrease in the SSA used in the DISAMAR radiative transfer model.